International Journal of Greenhouse Gas Control 82 (2019) 98–116

Contents lists available at ScienceDirect

International Journal of Greenhouse Gas Control

journal homepage: www.elsevier.com/locate/ijggc

Time lapse seismic analysis of the Tohoku-Oki 2011 earthquake

M. Landrø[a,*], S. Kodaira[b], T. Fujiwara[b], T. No[b], W. Weibull[c], B. Arntsen[d]

[a] NTNU, Department of Electronic Systems, Trondheim, Norway
[b] R&D Center for Earthquake and Tsunami, Japan Agency for Marine-Earth Science and Technology, Yokohama, Japan
[c] University of Stavanger, Department of Petroleum Engineering and Applied Geophysics, Stavanger, Norway
[d] NTNU, Department of Geoscience and Petroleum, Trondheim, Norway

ARTICLE INFO

Keywords:
Time lapse seismic
Earthquake monitoring
Seabed displacements

ABSTRACT

A detailed time lapse seismic analysis of subsurface movements is presented using seismic 2D lines acquired prior to and after the Tohoku-Oki earthquake offshore Japan in 2011. Estimated movements of the seabed from the time lapse seismic data corresponds well with estimations using bathymetric data. On the shelf, we find seabed subsidence of up to 8–9 m, and closer to the Japan trench, we find a seabed uplift of more than 10 m. Along the 100 km long 2D seismic line, we find alternating subsidence and uplift. We find horizontal displacements at the seabed that are significantly larger, up to 40–50 m, however these estimates are more uncertain. Close to the Japan trench, these horizontal displacements are practically opposite in direction (pointing towards the trench from both sides) and large (˜15 m). At the sediment-basement interface, we estimate vertical subsidence of two independent large blocks (each 4 km wide) to be up to 14 m. This means that the sediment package in this region has been stretched by 5–6 m. This type of overburden stretching is similar to hydrocarbon reservoirs that compact due to production and produce corresponding overburden stretching. Several examples of new faults, new layering and orientation of sedimentary layers are found. Implications for subsurface storage of CO_2 in areas close to subduction zones are also discussed.

1. Introduction

Co-seismic fault slip behaviour of the 2011 Tohoku-Oki earthquake has been intensively studied by seismological, geophysical, geological, geodetic and tsunami wave data. Although various models of co-seismic slip distributions (*e.g.,* Fujii et al., 2011; Lay et al., 2011; Ide et al., 2011; Satake et al., 2013) have been suggested, there is a general consensus that a large co-seismic fault slip of more than 50 m reached the trench axis of the central part of the Japan Trench. This large co-seismic slip generates a large seafloor displacement (Sato et al., 2011; Kido et al., 2011; Ito et al., 2011) which is considered to be the major cause of the large tsunami wave hitting the coastline of the eastern part of Japan. In addition to those studies, data from several marine geological and geophysical studies demonstrate more direct evidences showing trench breaching co-seismic slip (Fujiwara et al., 2011 *and* Kodaira et al., 2012).

Differential bathymetry measured before and after the 2011 Tohoku-Oki earthquake clearly shows that the sea floor on the outermost part of the landward of slope to the trench moved ˜50 m east-southeast towards the trench and ˜7 to 10 m upward (Fujiwara et al., 2011). The seafloor displacements terminate at the trench axis. Co-seismic structural changes of the sedimentary section above the plate interface at the trench axis are observed by visual comparison of seismic sections acquired along the same profile (Kodaira et al., 2012). The differential bathymetry and seismic data are the first direct evidences showing co-seismic fault rupture of a subduction zone where an earthquake breaches the seafloor at the trench axis. However, quantitative analysis of co-seismic structural changes near the trench in order to examine co-seismic deformation processes has not been performed so far, due to challenges related to time lapse analysis of the seismic data. Some of these challenges include variations in acquisition set up and positioning issues causing lower repeatability compared to conventional time lapse seismic surveys.

The main objective of this paper is to investigate if a detailed, quantitative time lapse seismic analysis of two datasets acquired before and after the earthquake, can reveal new insight into rock movements and changes in rock properties. For this purpose we reprocessed the two datasets, estimated seismic velocities independently for the two surveys, and obtained two similar data sets better suited for time lapse seismic analysis. With our background from 4D seismic analysis (Landrø et al., 1999; Landrø, 2001, 2015) and seismic imaging (Weibull and Arntsen, 2013), we want to explore how this knowledge can be

* Corresponding author.
E-mail address: martin.landro@ntnu.no (M. Landrø).

https://doi.org/10.1016/j.ijggc.2019.01.002
Received 27 July 2018; Received in revised form 23 November 2018; Accepted 3 January 2019
Available online 12 January 2019

used for improved understanding and mapping of earthquakes.

In the 2005 IPCC special report on carbon capture and storage (IPCC, 2005) there is a separate chapter on the geographical relationship between the sources of CO_2-emissions and storage opportunities. Areas considered as highly prospective are sedimentary basins far away from subduction zones. However, some of the next category of potential storage sites, characterized as prospective sedimentary basins that are close to major subduction zones, as for instance offshore Japan and Indonesia. Apart from one minor demonstration project (Tanaka et al., 2017) there are no CO_2-storage projects close to our study area. Our motivation for linking our time-lapse analysis of the Tohoku 2011 earthquake is therefore futuristic: Since the CO_2-sources in Japan are significant, there might be a need to store significant amount of CO_2 offshore Japan. In addition to this, a time-lapse seismic analysis of one of the largest recent earthquakes, is of general interest for other potential storage sites on earth.

In our analysis we will assume that most of the movements between the seismic surveys acquired in 1999 and 2011 is caused by the huge Tohoku-Oki earthquake in 2011. Other earthquakes that occurred within the timeframe between the monitor and base surveys are significantly weaker, but since the time interval between the two surveys is more that 10 years, we cannot disregard that some of the movements we have identified are not caused by the major 2011-event. Iinuma (2018) used GPS data recorded in Japan in the period from 1997 to 2016 and showed that earthquakes of less strength than the Tohoku were observable, but as minor displacement changes (order of 1 cm). The overall trend in his data was the long-term trend due to slow slip over 20 years.

2. Tectonic setting

The Japan Trench is a convergent plate boundary where the Pacific plate subducts beneath the volcanic arc of the northern Japan, and extends from the junction with the Kuril Trench at the north to the junction with the Izu-Bonin Trench at the south. The geological structures of the Japan Trench subduction zone have been well-studied by seismic surveys and ocean drilling since the last three decades. Based on the data from the seismic and the ocean drilling, previous geological and seismic studies commonly divided the forearc region of the Japan Trench into four areas, which consists of the deep sea terrace, the upper slope, middle slop and lower slope from landward to the trench axis (e.g., von Huene and Culotta, 1989; von Huene and Lallemand, 1990). The deep sea terrace is a gently deepened slope at water depth down to ~ 3 km, and continues to a rather steep upper slope extending from water depths of about 3 km to 5 km. The middle slope generally shows a terrace-like, locally narrow, gentle slope with water depth around ~5 km. At the trench-ward of the middle slope, the steep and rugged lower slop continues to the trench axis. The trench axis shows intermittent narrow and flat basin, which locally consists of graben-fill sediments. The oceanic crust entering the trench is characterized as clear horst-and-graben structure due to bending the subducted oceanic plate. The horst-and-graben structure seems to be growing even after the oceanic crust is subducted (Tsuru et al., 2002; Kodaira et al., 2017).

The results of ocean drilling combined with seismic images show Plio-Pleistocene and Miocene sediments that unconformably overlie the Cretaceous continental block at the shallow part of the deep sea terrace and the upper slope (Tamaki et al., 1990; Jolivet and Tamaki, 1992). The shallow part of the Plio-Pleistocene strata from the deep sea terrace to the upper slope are deformed by normal faults, which locally extend to the sea floor. Previous studies proposed that the normal fault system have formed due to tectonic erosion of the base of the overriding plate by subduction of a rough basement geometry of the oceanic crust, which cause a continental subsidence in the fore arc (von Huene and Lallemand, 1990;von Huene et al., 1994). However, the tectonic process to form the extension (normal faulted) structure in the fore arc region of the convergent plate boundary is still debated.

Table 1
Acquisition parameters for the MY101 (1999) survey.

Source	Airgun 9000 cu.in
Source depth	10 m
Shotpoint interval	50 m
Streamer depth	15 m
Receiver interval	25 m
Maximum offset	3445 m
Low pass cutoff	3 Hz
High pass cutoff	102 Hz
Time sampling interval	4 ms
Record length	13.5 s

A prism-shaped low-velocity wedge at the trench-ward end of the overriding block has been reported as a characteristic structure of the Japan Trench since von Huene et al. (1994) have shown its fine seismic image. The prism-shaped low-velocity wedge is roughly 20–30 km wide and 3–4 km thick with seismic velocities ranging between 2–3 km/s. Compilations of distribution of the prism-shaped low-velocity wedge show that those low-velocity wedges mostly developed at the norther part of the Japan Trench (i.e., north of 37.5 °N) (Tsuru et al., 2002; Kodaira et al., 2017). In the southern part of the Japan Trench, instead of the prism-shaped low-velocity wedge, a low-velocity (3–4 km/s) elongated sedimentary unit extends in the downdip direction along the plate boundary interface. Recent ocean drilling results show that the trench-ward tip of the prism-shaped low-velocity wedge mostly consists of pelagic sediments (Chester et al., 2013)

3. Data acquisition of 1999 and 2011 seismic data sets

The baseline 2D seismic (MY101) was acquired in 1999. Table 1 gives a summary of the acquisition parameters. A source array consisting of 6 identical subarrays each with a volume of 1500 cubic inches was used. The gun depth was 10 m, and the streamer depth was 15 m. The streamer length was 3600 m, and a shot point interval of 50 m was used. The receiver interval was 25 m, and a total of 144 channels were recorded. The monitor survey (D13) was acquired in May 2011, after the Tohoku-Oki earthquake. A summary of acquisition parameters is given in Table 2. A source array consisting of 4 identical subarrays with a volume of 1950 cubic inches was used. This means that the total source volume of the monitor survey (7800 cu. in.) is somewhat less than that of the baseline survey (9000 cu. in.). Hence we expect a somewhat weaker signal for the monitor survey (10% reduction). The gun depth was the same as for the 1999 survey (10 m), but the streamer depth was increased from 15 to 21 m. The streamer length for the monitor survey in 2011 was 5500 m, the receiver interval was 12.5 m and the total number of channels was 444. The location of the 2D seismic line (denoted D13 and MY101) is shown in Fig. 1. The difference in cable depths for the two surveys results in slightly different spectral compositions, due to the ghost effects. The source ghost spectrum is given by (Amundsen and Landrø, 2010)

Table 2
Acquisition parameters for the D13 (2011) survey.

Source	Airgun 7800 cu.in
Source depth	10 m
Shotpoint interval	50 m
Streamer depth	21 m
Receiver interval	12.5 m
Maximum offset	5415 m
Low pass cutoff	3 Hz
High pass cutoff	200 Hz
Time sampling interval	2 ms
Record length	18 s

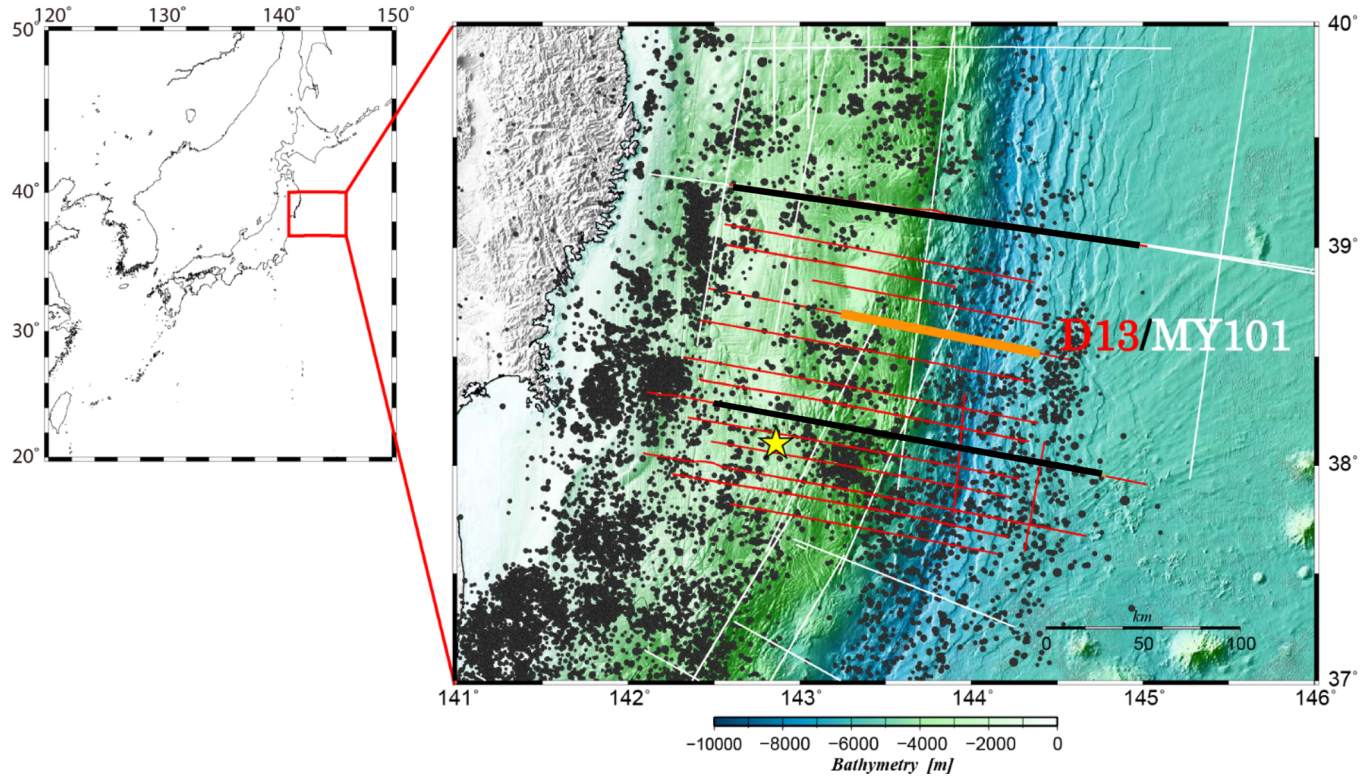

Fig. 1. Bathymetric map of the Japan trench showing the 2D seismic line (solid orange line) used in this study (D13/MY101) and two additional lines (solid black lines) that have also been repeated but not used in this study. The yellow star indicates the epicentre for the Tohoku-Oki 2011 earthquake. (For interpretation of the references to colour in this figure legend, the reader is referred to the web version of this article).

$$G_{source}(f) = \left| 2\sin\left(\frac{2\pi f z}{c}\right)\right| \quad (1)$$

Where f denotes frequency, z is the source depth and c is the water velocity. The source ghost spectrum is shown in Fig. 2, and is identical for the two surveys. The receiver ghost spectra will however be slightly different as shown in Fig. 2. Since the receiver depth is increased from the first to the second survey, the first notch in the receiver ghost spectrum is shifted from 50 to 37 Hz (assuming a water velocity of 1500 m/s). This difference means that there will be a significant difference between the two datasets for frequencies between 30 and 60 Hz. To some extent, it is possible to compensate for this by using Wiener-type match filters (as described in the next section). However, especially close to the receiver ghost notches (36.6 and 50 Hz) it is practically impossible to compensate for loss of data caused by the ghost notches.

4. Time lapse processing of the data

4.1. Preprocessing, regularization and key processing steps

Interpolation was used to make the 1999 and 2011 datasets conform to a common regular geometry. A 2D deterministic deconvolution (time and angle dependent) was used to modify the wavelet in the 2011 dataset, which contained significant bubble reverberations. The target wavelet used was a Ricker wavelet with a dominant frequency of 20 Hz.

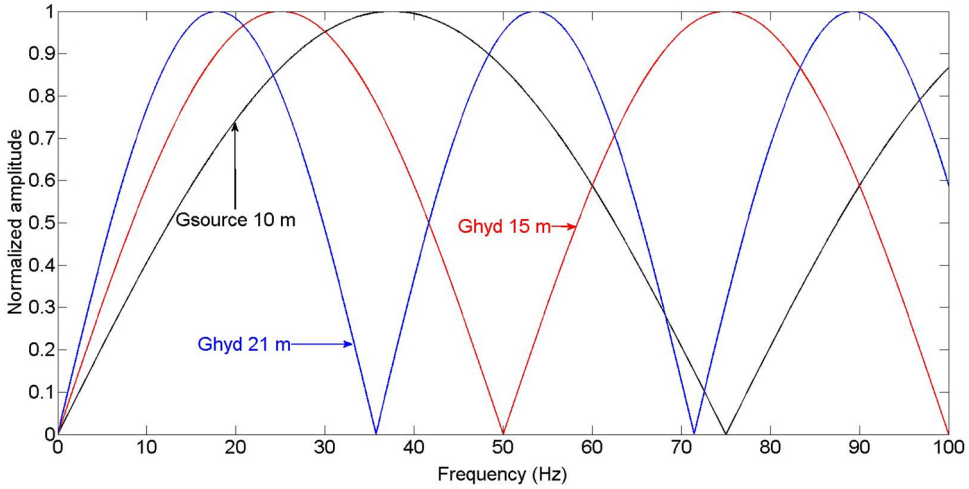

Fig. 2. Normalized source (black line) and receiver ghost spectra (red line for 15 m receiver depth and blue line for 21 m received depth). Notice that the 2011 data will have limited amount of data around 36 Hz and the 1999 data will have a similar loss of data around 50 Hz.

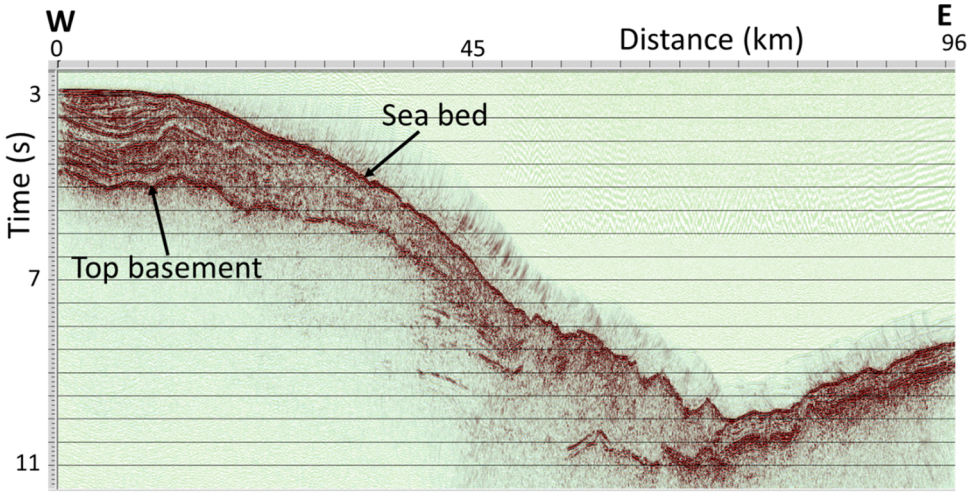

Fig. 3. The seismic 2D line (before the earthquake). (For interpretation of the references to colour in this figure legend, the reader is referred to the web version of this article).

Following this procedure, one global match filter was derived to match the 1999 dataset to the 2011 dataset. Totally 22,800 traces were used to compute an average Wiener filter. This filter was then applied to the 1999 dataset, in order to make it as similar as possible to the 2011 dataset. The data were then binned using a CMP (Common MidPoint) interval of 12.5 m, leading to 7740 CMP positions, with a fold of 36 traces within each CMP. The offset interval for the CMP gathers was 100 m. Velocities were picked independently for the two datasets using an auto-picker algorithm. The auto-picked velocities were reliable only down to the top basement reflection (Fig. 3). Where the signal to noise ratio was poor and where there were strong free surface multiples, the auto picked velocities were substituted by a constant stacking velocity of 2200 m/s. The picked velocities were smoothed laterally using a 500 m running average window.

The resultant two sets of stacking velocities were smoothed and used for prestack time migration of the respective seismic datasets. The reason for using two sets of stacking velocities for migrating the data is that the velocities found were significantly different between 1999 and 2011. Using only one velocity or an average velocity leads to a pronounced under or overcorrection of the prestack seismic gathers. This could in turn lead to large differences between the seismic images between 1999 and 2011, and mask the true time lapse effects. Another advantage of using two different velocity fields, is that the velocity differences contain information that can be used as an independent source of information in the analysis. The stacked version of the baseline survey from 1999 is shown in Fig. 3. The seabed reflection is clearly mapped, as well as the basement. The Japan trench is at the maximum water depth around 72 km in distance (measured from the start of the line).

4.2. Basic assumptions and precautions

Velocity variations in the water column are a major uncertainty in the time lapse seismic analysis. We tested both a 1% velocity increase and decrease in velocity between the two surveys (Fig. 5, bottom), and both tests lead to slightly more unrealistic estimates of the seabed uplift. Therefore, we assumed no changes in water velocity between the two surveys. This is in good agreement with the bathymetry data as shown in Fig. 5 (top); i.e., a general trend of variation of seafloor displacements estimated from the bathymetry and the seismic data shows a similar pattern.

For some parts of the seismic line (especially between 14 and 18 km) there are significant errors in source positions, up to 500 m. These positioning issues and how they impact the 4D seismic analysis are further discussed in Appendix B.

5. Geomechanical modeling and estimation of the dilation factor

The importance of geomechanics related to time lapse seismic studies was realized when the first 4D seismic results from the hydrocarbon chalk fields (Ekofisk and Valhall) in the southern North Sea came (Guilbot and Smith, 2002; Barkved and Kristiansen, 2005). Highly porous chalk is a weak reservoir rock and compaction larger than 10 m has been observed for the Ekofisk field, and a somewhat less seabed subsidence of up to 8 m (Guilbot and Smith, 2002). The fact that the reservoir compaction is larger than the seabed subsidence means that the rocks above the reservoir are stretched. The reservoir compaction is mainly caused by two effects in this case: First, the pore pressure decrease leads to compaction and second a chemical reaction between injected water and the chalk weakens the rock (water weakening), and this leads to compaction. The challenge for time lapse seismic analysis is that for rocks that undergoes either stretching or compaction, there are two unknown parameters: the thickness change and the velocity change. Landrø and Stammeijer (2004) showed that the relative time lapse seismic timeshift (dT/T) is directly related to the relative velocity change (dv/v) and the relative thickness change (dz/z) as:

$$\frac{dT}{T} = -\frac{dv}{v} + \frac{dz}{z} \tag{2}$$

Hatchell et al. (2005) and Røste et al. (2005) give a simple relation between the measured relative seismic timeshift (dT/T) and the stretching (dz/z) of the rocks:

$$\frac{dT}{T} = (1 + R)\frac{dz}{z} \tag{3}$$

where $R = -\frac{dv/v}{dz/z}$, dz represents the stretching of the rocks, z is the thickness of the overburden rocks, and R is an empirical constant often referred to as the dilation factor. v is the average P-wave velocity and dv is the change caused by stretching or compaction. Hatchell and Bourne (2005) find R-values ranging between 1 and 5 based on time lapse seismic data acquired in the North Sea. In a more recent study, Røste et al. (2015) find R-values up to 20 for overburden rocks at the Snorre field, North Sea. In this work we estimate timeshifts (right hand side of Eq. 2) directly from the time lapse seismic data, and then a simple geomechanical modeling based on Geertsmaa's equation (Geertsmaa, 1973) is used to estimate dz/z. An alternative way to estimate R-factors directly from time lapse seismic data is to use AVO (Amplitude Versus Offset) techniques as described by Landrø and Stammeijer (2004).

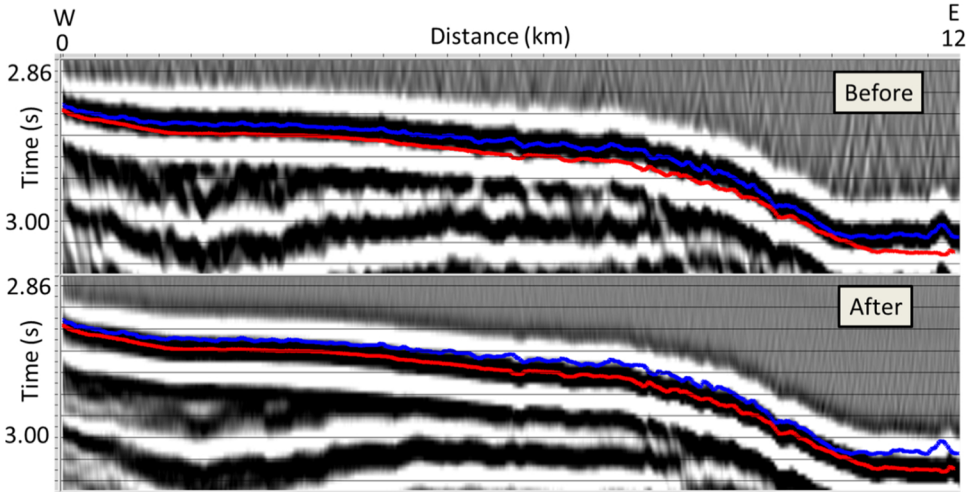

Fig. 4. The vertical movement of the seabed observed on the time lapse seismic data before (top) and after (bottom) the earthquake. The blue line represents the maximum peak pick before and the red line after. The average time shift is approximately 10 ms. Note that blue and red lines are plotted at the same positions in both sections, to clearly visualize the seismic traveltime shift between the two surveys for the seabed reflection. (For interpretation of the references to colour in this figure legend, the reader is referred to the web version of this article).

6. Results

6.1. Seabed displacement

Fig. 4 shows seismic sections covering the seabed reflection before and after the earthquake for the shelf (first 12 km of the line). The blue line represents the automatic picking of the maximum amplitude of the seabed reflection for the 1999-data, and the red line represents the same event for the 2011 data. An average time shift of approximately 10 ms is observed. Using the same automatic picking method for the whole line we observe not only vertical shifts, but also horizontal shifts.

Fig. 5 (top) shows a comparison of estimated vertical seabed uplift from bathymetric data (blue solid line) and time lapse seismic data (black solid line). We notice a good correlation between the two techniques. A 625 m long lateral smoother has been applied to both data sets. The time lapse seismic estimates are based on automatic picking of the maximum peak at the seabed for the base and monitor seismic datasets, followed by a direct subtraction. Conversion into seabed uplift is done by assuming a constant water velocity of 1500 m/s. The brown solid line shows the seabed position along the seismic line. It is inherently challenging to estimate error bars or uncertainties for the estimated seabed uplift. This it due to the fact that there are several systematic error sources. One obvious error source is that the water velocity may change between the base and monitor survey. This is discussed in detail in Appendix A. Based on this we have picked a value of +/− 1% to estimate the uncertainty related to varying water velocity. This uncertainty is shown as a grey shaded area in Fig. 5 (bottom). Uncertainties related to positioning errors and a non-smooth sea bottom is discussed in Appendix B. We performed a simple 3D seismic modeling exercise for a limited part of the line (the first 26 km) and used the positioning errors and the seabed topography in this area to estimate traveltime errors (Fig. B3). These traveltime errors were

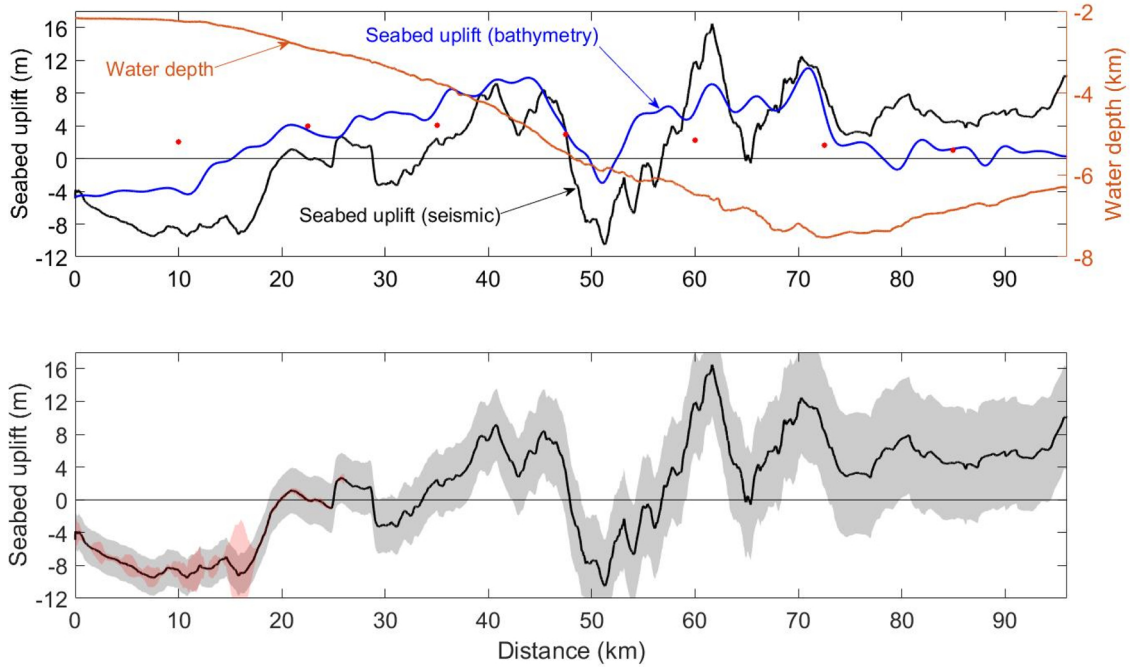

Fig. 5. Top: comparison between vertical seabed displacements estimated from bathymetric data (blue) and the time lapse seismic data (black). The seabed profile is the brown curve and the filled red circles are values taken from Fig. 6d in Jiang and Simons paper from 2016. Bottom: The estimated seismic displacements (black curve) and two types of uncertainty estimates shown as shaded fill. The grey shaded area represent a systematic water velocity change of plus or minus 1.5 m/s between the two seismic surveys, and the red shaded area represents errors estimated from 3D modeling of shot position errors and the seabed topography (see Appendix B). (For interpretation of the references to colour in this figure legend, the reader is referred to the web version of this article).

then converted to systematic errors in the seabed uplift estimations and are shown by the red shaded area in Fig. 5 (bottom). We notice that these positioning errors are less than the velocity induced errors apart for distances between 15 and 18 km.

Based on these tests and comparison to the bathymetric data shown in Fig. 5 (top), we concluded that the most probable situation is that the water velocity has not changed significantly between 1999 and 2011. To justify this choice further, we analyzed temperature and salinity profiles from the same area acquired in 1999 and 2011. The analysis (Appendix A) shows that the expected traveltime shifts caused by seasonal changes in water velocity are less than 3–4 ms, and therefore less than the maximum estimated time shifts which are up to 10–12 ms at the seabed and 50 ms at the top basement interface.

Jiang and Simons (2016) use a Bayesian framework to estimate seafloor uplift based on observed tsunami waveforms close to the Japan coast. If we compare our estimates of seabed uplift with those (shown by red circles in Fig. 5 (top)) presented by Jiang and Simons (2016) we observe that our results have higher spatial resolution. The result of Jiang and Simons is much smoother and contains less spatial variations compared to both the time lapse seismic estimates as well as the bathymetric results. It should be noted that the results of Jiang and Simons have been extracted directly from Fig. 6 in their paper, and that we have not received any numerical data directly from them. There is therefore an uncertainty associated with the red circles in our Fig. 5 (top) due to limited accuracy of picking correct values from the color bar in their Fig. 6.

Fig. 6 shows an example where horizontal movements are observable. By plotting the estimated seabed position for both seismic surveys, we see that the red line (representing the data after the earthquake) is shifted towards East for the area West of the Japan trench (between 60 and 73 km). For the area East of the trench (between 78 and 85 km) horizontal movement in the opposite direction is observed (towards West). A simple way to estimate horizontal and vertical displacements simultaneously is sketched in the insert of Fig. 6, where the horizontal displacement is simply approximated as finding the nearest position on the monitor data set with the same z-coordinate as the base data set. The vertical displacement is estimated in a similar manner: finding the vertical displacement directly (this is the same as the vertical displacement estimated in Fig. 5). As shown in the example, this simple method will not give correct displacement vectors. However, as a quick and first order estimate of 2D displacements it might serve as a useful tool, as shown in Fig. 7. In this figure we have multiplied the estimated displacement vectors by 50 for visualization purposes. We notice vertical displacements at the shelf, followed by horizontal movements towards West between 28–32 km, towards East between 36–48 km and 55–75 km. At the opposite side of the Japan trench, we observe horizontal displacements towards West (80–92 km).

6.2. Variations in the sedimentary unit

At the continental shelf we find that the sedimentary unit beneath the seabed is stretched. This stretch is not constant, but is found to be discontinuous and corresponding to vertical movements within specific fault zones. This is illustrated in Fig. 8, where we observe two distinct areas (4.3–8.3 km and 10.5–14.5 km) where the subsidence at top basement and corresponding vertical stretch is found to be particularly pronounced. In areas where a strong subsidence is observed, we typically find that the seabed subsidence is less than at the basement level. This effect is illustrated in Fig. 9 (bottom) where a stretching of the sedimentary package is estimated. Time shifts of the order of 40–45 ms are observed in these regions. In this case we cannot simply convert such time shifts directly into vertical displacements, since the stretching of the sediments leads to an unknown velocity decrease. We are faced with the challenge that we have two unknows (velocity change and vertical stretch) and one measurement: time shift. A common way to solve this ambiguity is to introduce an empirical factor (the *R*-factor or the dilation factor) relating the two unknowns and use geomechanical modeling to estimate it (Section 5). Using geomechanical modeling (Geertsma, 1973; Fjær et al., 2008) in our case, we can model displacements as shown in Figure X, we find an average *R*-factor equal to 6.7, and if this factor is used, we find that the seabed subsidence and the subsidence of the top basement are similar, but different, as shown in Fig. 9a. The difference is more clearly presented in Fig. 9b where the estimated stretching of the sedimentary unit is shown. We recognize the two fault zones related to subsiding areas (4–8 and 10–14 km). It should be stressed that the existence of these faults is based on interpretation of the time lapse seismic data. We do not know the direct cause of these faults, one possible mechanism could be horizontal stretching. Assuming that the *R*-factor is constant and equal to 6.7 for the overburden, we can estimate the overburden velocity changes (using Eq. 3 and the definition of *R*). Fig. 9c shows a comparison between the velocity changes estimated from the timeshifts (black line) and the average stacking velocity difference (red line) estimated from conventional velocity analysis of the two seismic data sets. We observe that there is a reasonably good correspondence between the two ways of velocity change estimation within the subsidence zones (marked by vertical dashed lines in Fig. 9b). A rough estimate of the average deviation is 15 m/s within subsidence zone 1 and 10 m/s for subsidence

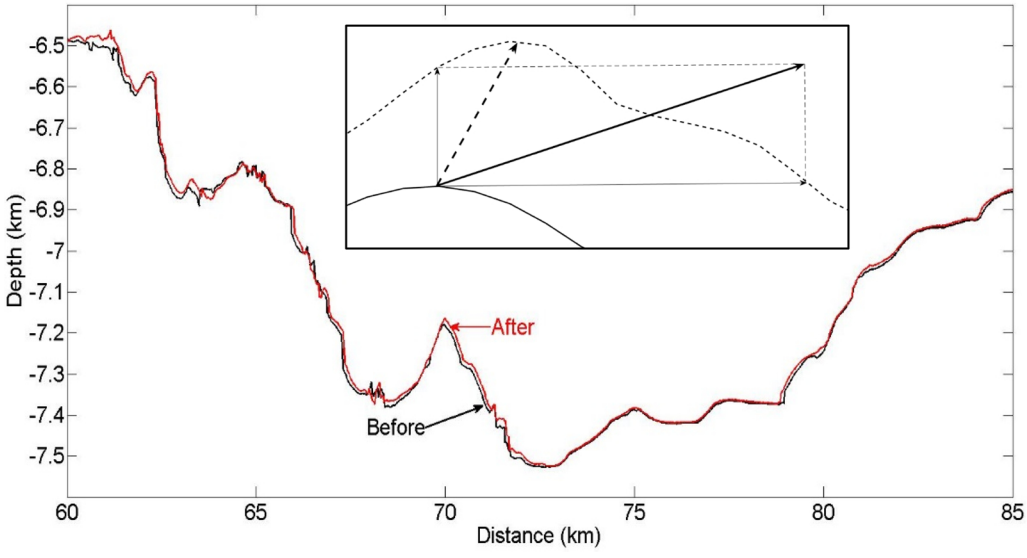

Fig. 6. Estimated water depth based on automatic picking of the seabed reflection in time, assuming a constant water velocity of 1500 m/s. Notice the horizontal shift of approximately +60 m in the region between 60 and 70 km, and −40 m in the region between 78 and 85 km. Inserted: example showing the error introduced by the simple vector computation of displacement (solid arrow) versus the most likely one (dashed arrow). The solid and dashed curved in the inset represent the seabed position before and after the earthquake, respectively.

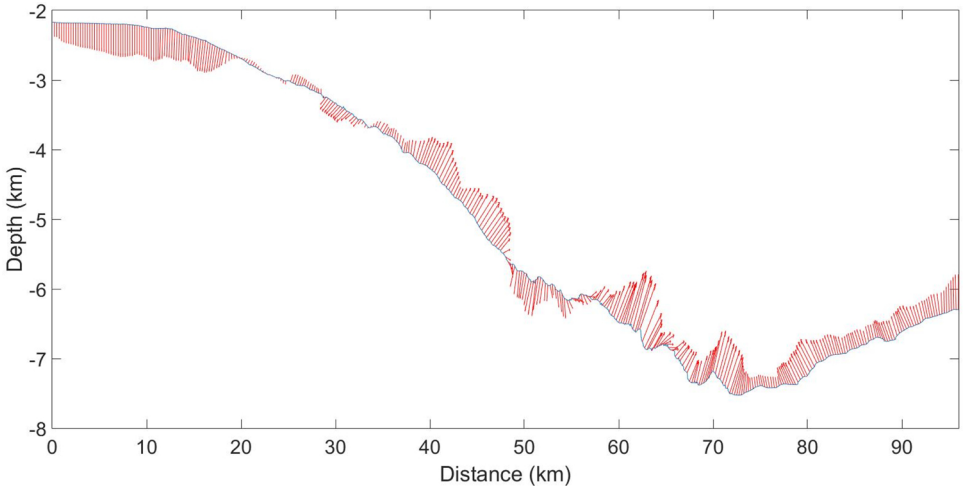

Fig. 7. Estimated seabed displacement vectors (red arrows). Note that the vertical scale is exaggerated, so that the angles of the displacement vectors appear more vertical than they actually are. The displacement vectors have been multiplied by 50 for visualization purposes. (For interpretation of the references to colour in this figure legend, the reader is referred to the web version of this article).

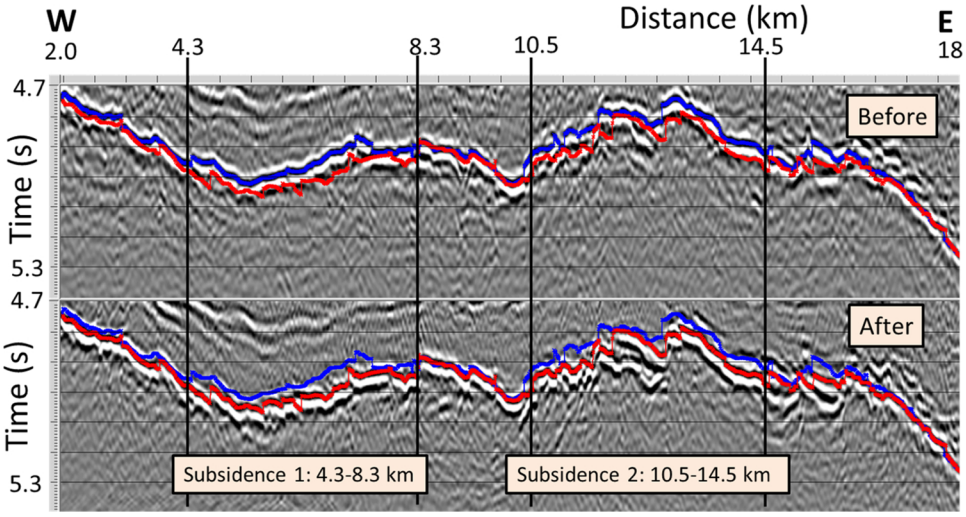

Fig. 8. a Subsidence between 4 and 8.5 km and 10 and 16 km for the top basement. Blue and red lines show interpreted top basement before (top) and after (bottom) the earthquake. The top basement is first interpreted on the top figure as a blue solid line. Then this interpretation is copied to exactly the same position on the lower figure, then the top basement is interpreted on the lower figure as a red line, and copied into the upper figure. Notice the significant timeshift for the two subsidence zones, up to 50–60 ms. (For interpretation of the references to colour in this figure legend, the reader is referred to the web version of this article).

zone 2. However, outside these subsidence zones there are significant differences between the two estimation methods. It should be stressed that the uncertainty related to stacking velocity changes are significant, probably of the order of 25–50 m/s. There are also significant uncertainties related to the geomechanical modeling, for instance the assumption of a cylindrical symmetry, as well as the estimate of the radius of the cylinder.

Fig. 10 (bottom) shows the estimated difference in stacking velocities between the two seismic surveys. As expected, we find a velocity decrease at the shelf area (0–20 km). However, for most of the slope towards the Japan trench, we find a velocity increase (20–50 km). For the area close to the trench (50–85 km) we observe a velocity decrease for the upper half of the sedimentary unit, followed by a velocity increase. It should be stressed that these velocity estimation is based on an automatic picking method, not influenced by interpretation or velocity picking by hand. However, it should be noted that if the automatic method fails, the velocity is simply assumed to be 2200 m/s. This has a minor effect on the final velocity field.

Close to the trench axis, where the sediment package is relatively thick, we observe alignment of some of the layers in an upward-East direction, as shown in Fig. 11. We notice that some of the horizontal interfaces (marked 1 and 2) on the figure are less pronounced and hard to interpret after the earthquake. Furthermore, some of the upward dipping (towards East) interfaces are more pronounced and stretch further towards the seabed after the earthquake (marked by 3 and 4 on the figure). This alignment is illustrated by the green arrows on the lower figure. A detailed investigation of event 4 is shown in Fig. 12, demonstrating that the dip has increased somewhat after the earthquake.

Approximately 10 km East of the trench axis, we find an area where the estimated *R*–factor (or the dilation factor) is negative. To our knowledge, this has not been observed for compacting or expanding hydrocarbon reservoirs, and hence we consider this as an anomaly. We find that the seabed timeshift is negative, while the top basement timeshift is close to zero. We interpret this as a combination of vertical compaction and horizontal stretching. It is likely to assume that the seabed uplift is caused by a vertical force from below. However, to explain the increased traveltime through the sediment package, we need an overall velocity decrease. So a combined effect of horizontal stretching and a somewhat less vertical stretching might explain the observed timeshifts and overall velocity decrease in the sediments. The horizontal stretching causes a decrease in P-wave velocity and the vertical compaction causes a negative vertical strain, yielding a negative dilation factor. Geomechanical modeling yields an *R*-factor equal to approximately -16. The sediment package is relatively thin in this area, only 0.5 km.

An important and surprising result from the analysis of movements within the sedimentary units is the small-scale (less than a kilometer) variations. Based on the time lapse seismic data we interpret vertical movements of several meters and larger horizontal movements. Due to a complex fault pattern and organization of the sedimentary units, our analysis indicate huge local variations and movements in opposite

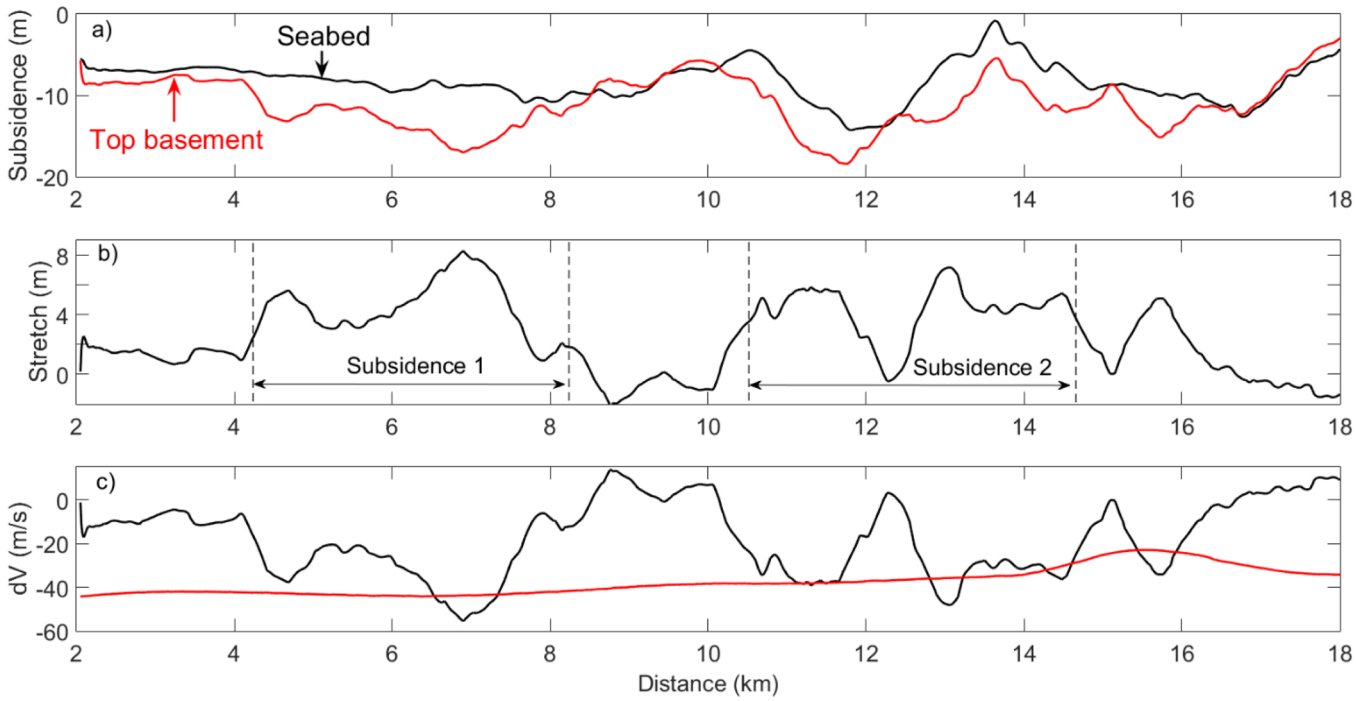

Fig. 9. a) Estimated subsidence at seabed (black solid line) and top basement (red solid line). b) Estimated stretch of the sediments, assuming an *R*-factor of 6.7. The two subsidence zones are indicated by dashed vertical lines. c) Comparison of velocity change estimates based on time lapse seismic timeshifts and assuming a constant R-factor of 6.7 (solid black line) and estimated average change in stacking velocities (red solid line). Notice that the two velocity change estimates show less deviation within the two subsidence zones. (For interpretation of the references to colour in this figure legend, the reader is referred to the web version of this article).

directions. We think these details are extremely hard to model and hence, time lapse seismic analysis can be used to achieve more detailed knowledge about earthquakes occurring close to subduction zones. Furthermore we see that time lapse seismic data has the potential to reveal detailed movements at the sedimentary-basement interface, and that these details are smeared out at the top of the sedimentary unit.

7. Implications for subsurface storage of CO_2 near subduction zones

Several authors have discussed the influence of earthquakes on subsurface storage of CO_2. Zoback and Gorelick (2012) argues that even small to moderate earthquakes threaten the seal integrity of a CO_2 storage site. Juanes et al. (2012) argued that there is no geologic evidence that seismicity causes fault leakage that would render large-scale storage of CO_2. One argument given by Juanes et al. is that there is still

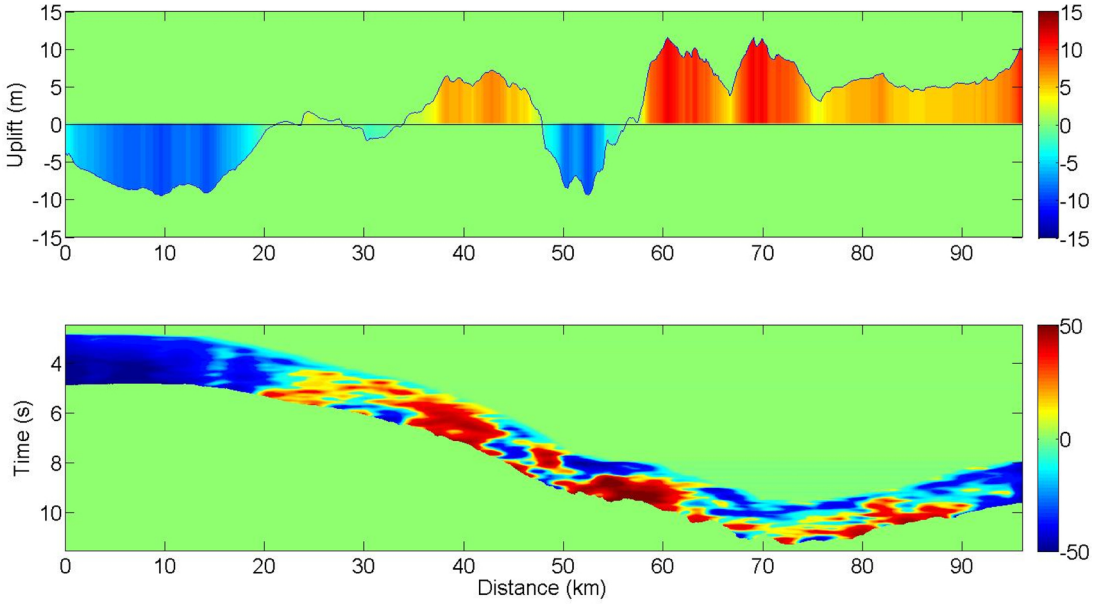

Fig. 10. Estimated vertical uplift at seabed (top) and difference in estimated stacking velocities (bottom) from the time lapse seismic data. Notice dominantly increased velocities for the slope between 25 and 60 km. There is a good correlation between velocity changes and seabed uplift for the first 50 km, but less correlation for large water depths (between 50 and 96 km).

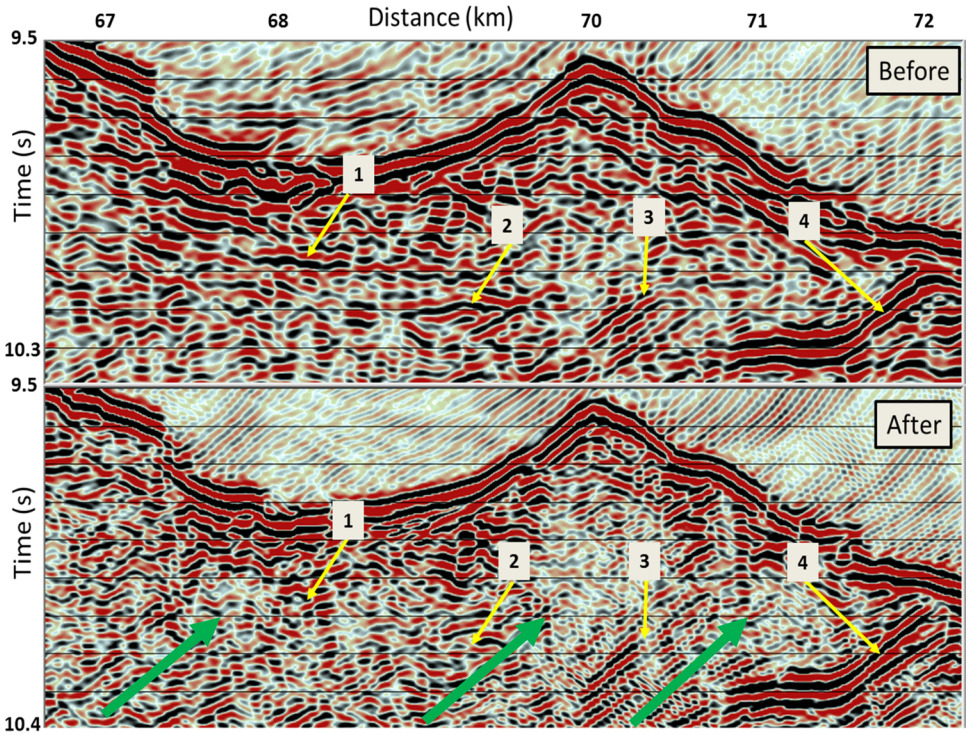

Fig. 11. Zoomed time lapse seismic close to the trench axis. Notice compression effects: Flat reflections (1 and 2) disappearing after the earthquake, and dipping reflections (3 and 4) showing increased lengths after the earthquake, aligning with the dominant sediment flow direction. Direction of rock movements are indicated by green arrows. (For interpretation of the references to colour in this figure legend, the reader is referred to the web version of this article).

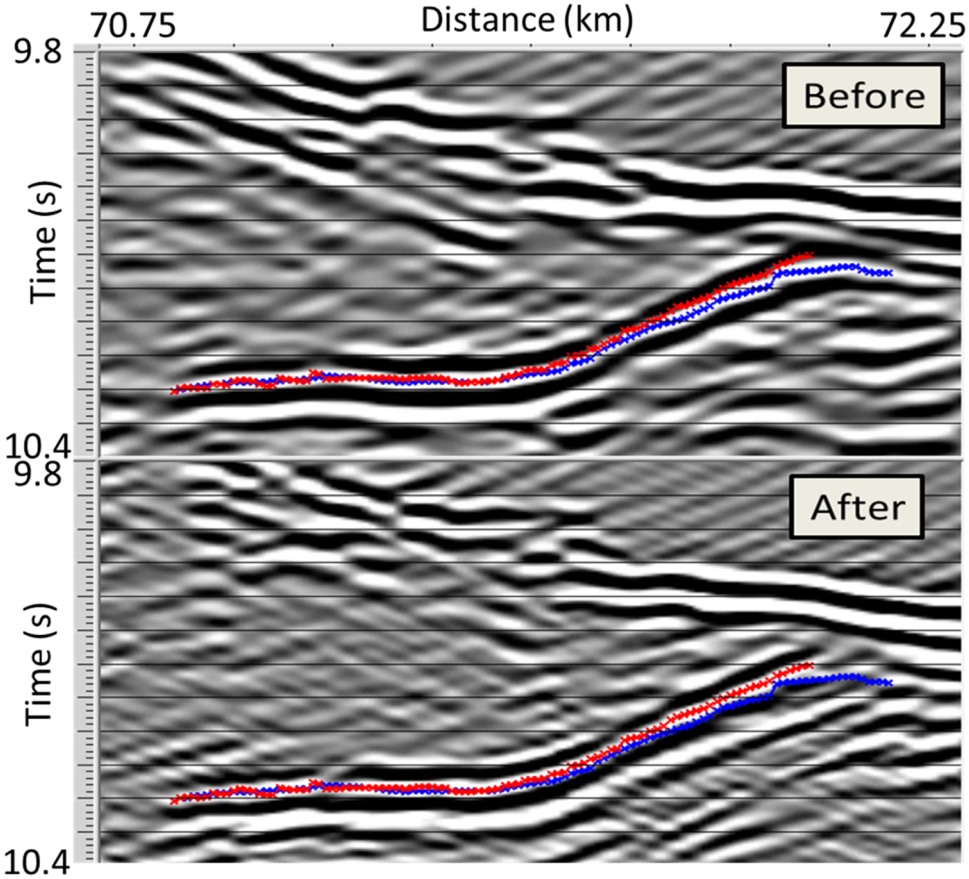

Fig. 12. Zoomed detail of the seismic data before (top) and after the earthquake demonstrating horizontal compression: the dip is increasing (red line) after the earthquake. (For interpretation of the references to colour in this figure legend, the reader is referred to the web version of this article).

large quantities of natural gas that is still present in the subsurface. Verdon (2014) finds that 99% of earthquake events related to fluid injection close to hydrocarbon fields occur within a radius of 20 km from the injection well. Verdon states that an induced event triggered well below the CO_2 storage volume will impose less risk for leakage as an event in the sealing caprocks. Furthermore, Verdon stresses the importance of mapping faults close to and below the CO_2 storage reservoir.

There is one CO_2-storage demonstration project being conducted in Tomakomai, Japan, approximately 500 km NorthWest of the seismic line investigated in this paper. Tanaka et al. (2017) describes that this project will store approximately 100 ktonnes of CO_2 per year into a sandstone layer at approximately 1 km depth. The injection well is drilled from the harbor area in Tomakomai into an offshore area approximately 3 km away. This project is monitored using onshore and offshore downhole seismometers, seabed seismometers and conventional 4D seismic. Another upcoming CCS-project is the Gundih pilot project in Indonesia, where the plan is to inject CO_2 into the Ngrayong sandstone formation at approximately 1 km depth (Tsuji et al., 2014). The Gundih field is located in North Java, approximately 360 km North of the Sunda trench, so this is also an example of a CO_2 injection project not too far from a major subduction zone.

Røste et al. (2007) give one example of fault reactivation interpreted from time-lapse seismic data above a producing oil reservoir offshore Norway. From Fig. 8 it is evident that there are significant time shifts that are observed between 4.3 to 8.3 km and between 10.5 and 14.5 km. We estimate the vertical displacement between 4.3 and 8.3 km to be roughly 15 m at top basement, and that the corresponding subsidence at the seabed is roughly 10 m, indicating a stretch of the sedimentary rocks of approximately 5 m. Outside this zone, this stretch (see Fig. 9c) is practically zero, suggesting fault reactivation close to 4.3 and 8.3 km, respectively. It should be noted that these vertical movements are at the continental shelf, some 50–60 km away from the trench axis. Vertical movements of the order of meters within a sediment column, does not necessarily mean that a CO_2-storage volume situated 1–2 km below seabed will leak. However, the abrupt lateral changes that is observed from Fig. 8, is a strong indication that close to vertical faults might be created or reactivated by deep earthquakes. Chu et al. (2011) estimated that the Tohoku earthquake originated from a small thrust event at a depth of 21 km, that a few seconds later, evolved into a slower extremely large slip event. Juanes et al. (2012) argue that the rheological properties of shallow sedimentary formations usually allow them to undergo substantial deformation without establishing leaking pathways or localized faults. From this work, we cannot conclude that new faults have been activated within the sediments by the Tohoku earthquake. However, both vertical and horizontal movements of the seabed as observed from time lapse bathymetry and seismic (Fig. 5) show relatively abrupt variations along the profile. Close to the sediment-basement interface these lateral variations are more pronounced. Fig. 9 b shows the estimated stretching of the sediment column caused by the earthquake, and within the two subsidence zones, this stretch is up to 5–7 m, which is significant.

Based on these observations it is very hard to judge whether large vertical and horizontal movements might cause leakage from a CO_2 storage site close to an active subduction zone. Detailed geomechanical modeling that is beyond the scope of this work might give a deeper insight into if leakage is likely to occur given that a major earthquake like the Tohoku occur at a given distance from a CO_2 storage site. As pointed out by Verdon, a detailed and comprehensive mapping of the storage reservoir as well as the underlying geology including pressure distributions and fault patterns is crucial in such cases.

8. Discussion

In the processing of the time lapse seismic data, separate velocity tables were calculated for the two datasets. This was done using an automatic picking procedure, and it was necessary to flatten the pre-stack seismic gathers. Due to the limited offset range (0–3.6 km), the velocity analysis is more unstable and less reliable for deep horizons, and especially close to the Japan trench, where the water depth is close to 7 km. This means that the offset/depth ratio is only 0.5 close to the trench compared to 1.8 at the shelf. Hence, we should bear in mind that the accuracy of the velocity differences decreases as water depth increases. Fig. 10 shows a comparison between the estimated seabed uplift and the estimated velocity changes. For comparison, we have used a slightly longer smoothing window for the seabed uplift curve compared to that shown in Fig. 5. We notice a good correlation between seabed uplift and velocity change for the first 50 km. Beyond this point there is no clear correlation between the two estimates. This might be caused by the increased inaccuracy of the velocity estimates with depth. Another cause might be variation in horizontal stretching along the line.

There are several uncertainties and precautions that should be addressed related to this work: First, the repeatability of these data is not as good as time lapse seismic data acquired for the purpose of monitoring subtle changes in a hydrocarbon reservoir. For instance, the position of both the air gun sources and the streamers is not very accurate, and therefore we expect less repeatable data, and the quantitative results should be handled with care. On the other hand, the estimated changes in both velocity and timeshifts are one order of magnitude higher than those normally observed for conventional 4D seismic surveys. We have tested how robust our estimates are with respect to for instance positioning errors and changes of for instance water velocity between the two surveys, and our conclusion is that our results are robust to such changes.

Another observation supporting the assumption of no or minor velocity changes in the water layer is that we observe a *positive* timeshift between the seabed reflection and the top basement interface at the shelf (first 20 km of the seismic line). As described in section 5, this corresponds to a stretching of the sedimentary rocks in this region, and the estimated *R*-factor (that is well known from reservoir monitoring studies of compacting hydrocarbon fields (Røste et al., 2005 *and* Hatchell et al., 2005) is found to be close to 6.7. This is in good agreement with previous work for sedimentary rocks. A change in water velocity will alter this value, and especially a slight increase in water velocity leading to no subsidence at the shelf, will be very unlikely, since we observe a stretching of the sedimentary rocks in this area.

Osdal and Landrø (2011) discuss methods for estimating velocity and water column thickness variations directly from time lapse seismic data. Seasonal variations in water velocity measured at a field (offshore Norway) where the water depth is 380 m are of the order of 3–4 m/s in average. The velocity variations are largest for the upper 50 m, and tend to decrease with water depth. Water velocity variations are mainly caused by temperature and salinity variations (Mackenzie, 1981). Lee and Cox (1966) uses measured temperature profiles offshore California to show that the temperature variations decrease significantly with water depth typically from 0.5 °C at 85 m to 0.014 °C at 2500 m water depth. Hence, it is reasonable to assume that seasonal velocity changes for the whole water column in our case is minor, and probably less than +/- 1.5 m/s. This is further discussed in Appendix A.

The usefulness of repeated long 2D seismic lines were tested at the Troll field offshore Norway using 8 2D lines acquired in 1997 and repeated in 2002 (Eiken and Tøndel, 2005). Timeshifts up to 0.6 ms were estimated for an interface below the gas reservoir (situated at approximately 1500 m below sea level) with an accuracy of 0.1 ms. There are other examples of time lapse analysis of repeated 2D seismic data (Landrø, 2011; Zadeh and Landrø, 2011) demonstrating that especially timeshift analysis is robust despite significant variations in shot and streamer positions. Another example where 2D and 3D time lapse results are compared can be found in Bergman et al. (2011). Unfortunately the 2D seismic line is not intersecting the time lapse seismic

anomaly caused by the CO_2-injection at Ketzin (Germany). However, this study confirms that the 2D time lapse seismic results are in agreement with the 3D results.

We think it is a good idea to acquire a third survey in the same area, using the same acquisition parameters as in 2011, in order to investigate potential changes in for instance stress or rock movements between 2011 and present.

A major shortcoming of this study is the lack of 3D seismic data. Especially when it comes to estimates of rock volumes, the uncertainty is large. Our plan is to process the two remaining lines shown in black in Fig. 1, and from these results try to at least get an indication of crossline stability or non-stability with regard to the results obtained so far. Furthermore, we think that a similar analysis for the other two lines might serve as an input to a 3D tsunami modeling, which can be compared to observations of the tsunami wave from 2011.

We interpret that the earthquake has caused a significant stretching (up to 7 m) of the relatively thick (2 km) sediment package on the Japan Shelf. This amount of stretching is varying abruptly along the seismic section, indicating that new faults are formed or reactivated. This means that the risk of establishing leaking pathways from a CO_2 storage site within the sediments is increased. However, since most CO_2-storage projects within soft sediments use an injection pressure which is gentle or low, the risk of a blow-out like event from such a site is negligible. Hence a recommendation for CO_2-storage within such formations is that the injection pressures should be kept as low as possible, similar to that used on Sleipner, offshore Norway (Arts et al., 2008, and Landrø and Zumberge, 2017). For the current Tomakomai CCS demonstration project (Tanaka et al., 2017) this is the case: The injection pressure is slightly above the hydrostatic pressure within the sandstone layer where CO_2 is injected. In addition there are clastic sediments including sandstone and siltstone above the mudstone cap rock layer in this case, which will further diminish the risk for CO_2 leakage into the sea.

9. Conclusions

Time lapse seismic analysis of two 2D lines crossing the Japan trench approximately 120 km North-East of the Tohoku-Oki earthquake epicenter shows clear evidence of fault slipping, extending all the way from the epicenter to the trench axis. From the time lapse seismic data we estimate an upward movement of the seabed of approximately 10–15 m close to the trench axis. Our observations fit with bathymetry data from the same area. Closer to the shelf, approximately 60–70 km West of the trench axis a seabed subsidence of approximately 7 m is found. In the same area (which is 20 km in length), a corresponding subsidence of the top basement interface (approximately 2 km below the seabed) is estimated to be around 13–14 m. This estimate is based on observed timeshifts at this interface combined with geomechanical modeling. Estimated dilation factors (relative velocity change divided by vertical stretch) in this area is around 7, which fits nicely with observations from compacting hydrocarbon reservoirs. This subsidence correlates well with an estimated decrease in P-wave velocity of approximately 40 m/s in the area. East of the trench axis, we find an area where the estimated dilation factor is negative. This is most likely due to a combination of vertical compaction and horizontal stretching. The horizontal stretching causes a decrease in P-wave velocity and the vertical compaction causes a negative vertical strain, yielding a negative dilation factor.

Along the 100 km seismic line, we identify alternating areas (approximately 10 km in length) undergoing horizontal stretching and compaction close to the seabed. The correlation between horizontal stretching and compaction and observed velocity changes is not as clear as for the subsidence zone at the shelf. The two seismic data sets used in this study are not dedicated time lapse data sets aiming for a high degree of repeatability between the two surveys. Despite this, the quantitative results obtained from this study indicate that dedicated time lapse seismic surveys in this and other seismically active areas will be highly useful.

Acknowledgments

The Norwegian Research Council is acknowledged for financial support (Grants 228400 and 254748). A part of this study was supported by KAKENHI Grants-in-Aid for Specially Promoted Research, number JP26000002, and for Scientific Research (S), number JP15H05718, from the Japan Society for the Promotion of Science. Raw seismic data are available from authors upon request. We want to thank Jiro Tanaka for discussions.

Appendix A. Seasonal changes in water velocity

There are vertical profiles of temperature and salinity (XCTD-data) available from the area close to the 2D seismic line used for this study. We used these data and the UNESCO equation (Chen and Millero (1977), Fofonoff and Millard (1983) and Wong and Zhu (1995)) to estimate the water velocity as a function of depth for various calendar times. Fig. A1 shows the velocity difference versus depth between the period 1 May to 31 May 2011 and the period 15 August to 15 September 1999. Before taking the difference between the two velocity profiles we averaged over several geographical locations in the area. Fig. A1 shows the velocity difference between 2011 and 1999 (blue curve) and the corresponding cumulative average velocity difference (red curve). We notice that the average velocity difference for the first kilometer is less than 1 m/s. As another example we averaged the velocity difference over all years between 1999 and 2011, as shown in Fig. A2. Also here, the cumulative average velocity difference at 1 km is relatively small, and less than 4 m/s. If we convert this into traveltime shift we find that an average velocity change of 4 m/s corresponds to a time lapse time shift of $dt = \frac{2z}{v}\frac{dv}{v} = 3.6ms$. This is less than the maximum estimated time shifts from the time lapse seismic analysis which are more than 10 ms for the seabed interface and more than 50 ms for the top basement interface. We realize that this is not a proof that water velocity changes might be neglected, however, it is an indication that this effect is probably not the main time lapse signal in our analysis.

Appendix B. Time-lapse processing of the MY101 (1999) and D13 (2011) seismic surveys

The two 2D marine seismic surveys from 2009 and 2011 were not originally designed to be used for high-precision time-lapse purposes. The repeatability of the source-receiver positions are not perfect and for parts of the survey there are considerable cable feathering problems.

Fig. B1 illustrates the former problem and shows the cross-line shot position error as a function of distance along the line. We observe a large deviation between 11.5 and 17 km, where the actual cross-line offset is as high as up to 500 m. However, the typical error in the cross-line direction is much less and generally less than 100 m. The cable feathering problem is illustrated in Fig. B2, which shows the cross-line offset distribution for the MY101 (1999) survey. The D13(2011) survey has similar problems. As shown by Nedimovic and West, (2003) cable feathering can potentially cause unacceptable changes both in traveltime and amplitude unless taken into account in the processing sequence. There are also differences between the two surveys in the cable length and cable depths causing further complications for the processing of the two surveys.

It is clear that we cannot expect to produce accurate time-lapse amplitude maps of the type routinely produced in conjunction with hydrocarbon exploration (Landrø, 1999). However, by reducing ambitions and concentrate on the travel time differences between the two datasets we should still

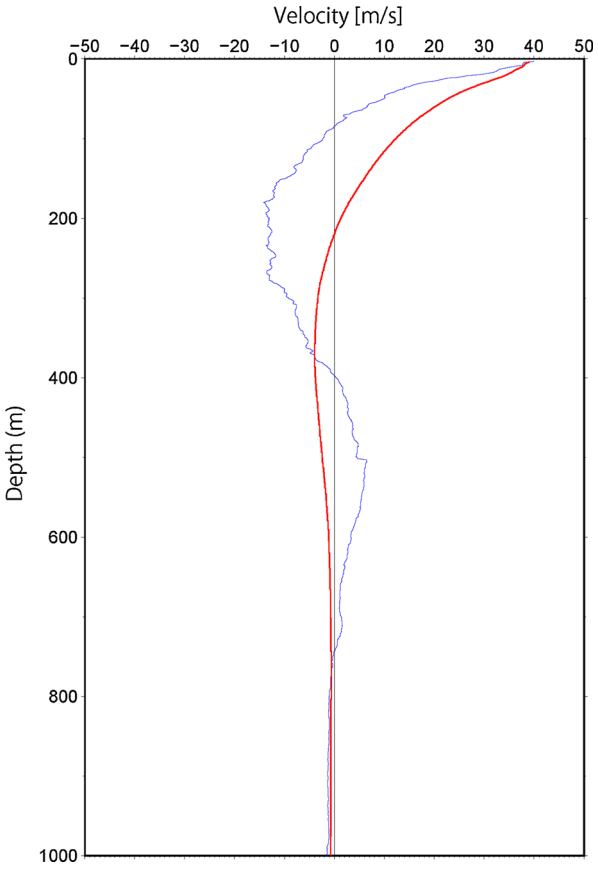

Fig. A1. Estimated water velocity difference between May (1st to 31st) 2011 and September (15th August to 15th September) 1999 (blue curve). The red curve shows the corresponding cumulative average velocity change. Notice that the velocity change is less than 1 m/s at 1000 m depth. (For interpretation of the references to colour in this figure legend, the reader is referred to the web version of this article).

be able to extract meaningful information about the subsurface. A mitigating circumstance is the fact that the cross-line dip in the area is quite small, reducing the impact on travel times from errors in the source-receiver positions.

The processing sequence can be summarized as:

1 Interpolation of shots to a nominal geometry
2 Shot designature
3 Matching of the MY101 (1999) and D13 (2011) surveys at the shot level.
4 Velocity analysis
5 Kirchhoff prestack time migration
6 Final output

The first step of the processing sequence was designed to minimize the impact of cable feathering and differences in source-receiver geometry between the two surveys. In principle a 2D seismic line with significant cable feathering must be processed as if it were a 3D shot line. The most straightforward approach is to use a 3D interpolation scheme taking the true 3D receiver and source geometry into account and outputting interpolated data along the 2D survey line. We use a version of Shepard's algorithm (Shepard, 1968) to perform the interpolation. Before interpolation the input data is NMO-corrected with the water velocity. The NMO-correction is backed off after interpolation. This compensates somewhat for offset errors and increases the accuracy of the interpolated data.

To verify the interpolation we simulated the 1999 survey using the true source-receiver positions with a 3D finite-difference modeling program. The velocity model was constructed using bathymetry data from the area around the survey line. The synthetic data was then prestack time migrated and the travel time error was measured from the migrated sections. Fig. B3 shows that the time shift error is close to 2 ms for most of the survey, except for two specific areas where it reaches 8 ms.

Designature of the shots were performed to remove the effect of the air gun bubble. A synthetic dataset was simulated using a point source in a half-space with a free surface. This was used as the desired wavelet in a 2D F–K deconvolution approach to produce a debubble filter. Fig. B4 shows an example of the input and desired output. The final filter used was taken as the average of a number of filters to avoid overfitting. Fig. B5 shows an example of the application of the filter to a shot record.

After interpolation of shot records and debubble a single global match filter was designed to match the MY101 (1999) dataset to the D13 (2011) data. The global match filter was based on an average of individual match filters for all shots. The match filter is shown in Fig. B6 and Fig. B7 shows an example of the application of the filter.

A standard velocity analysis with autopicking (see Appendix C) was used to derive velocity models for the two datasets. A smoothing filter with an aperture of 500 m was used for smoothing of the velocity field.

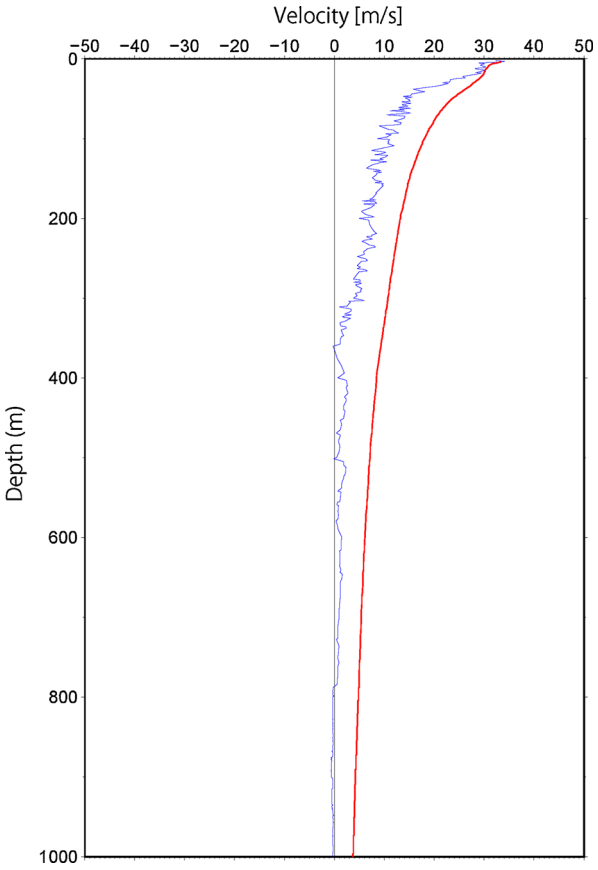

Fig. A2. Estimated water velocity difference between May (1st to 31st) averaged over all years from 1999 to 2011 and September (15th August to 15th September) for the same years. The red curve shows the corresponding cumulative average velocity change. Notice that the velocity change is less than 4 m/s at 1000 m depth. (For interpretation of the references to colour in this figure legend, the reader is referred to the web version of this article).

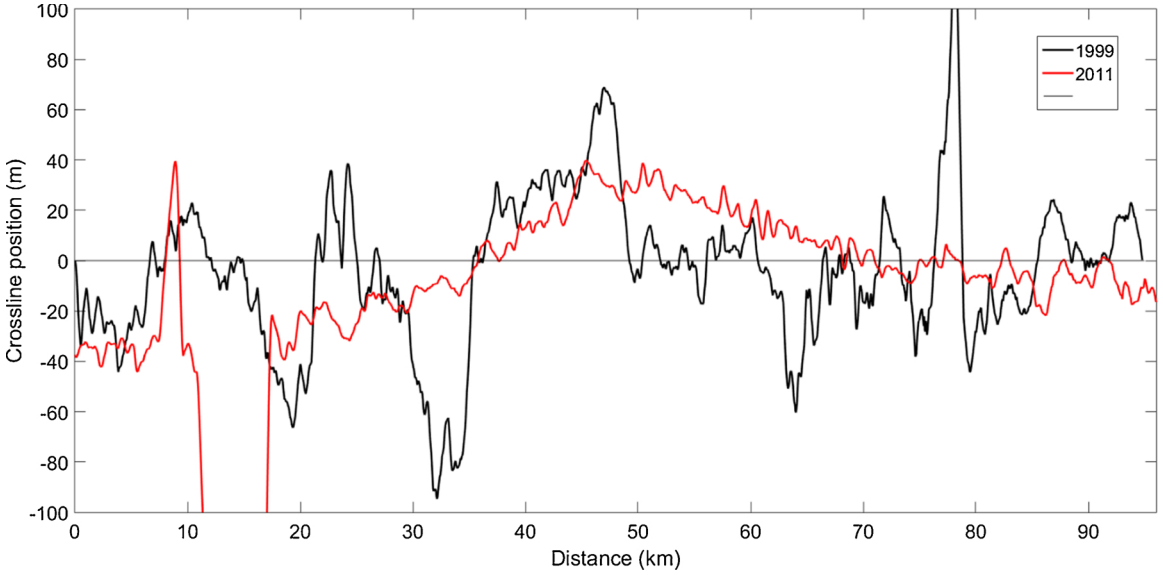

Fig. B1. Shot positions relative to a straight line (at zero) for the 1999 (black) and 2011 (red) data. There is a large mis-positioning between 11.5 and 17 km, up to 500 m. Apart from this, the positioning errors are less than 100 m. (For interpretation of the references to colour in this figure legend, the reader is referred to the web version of this article).

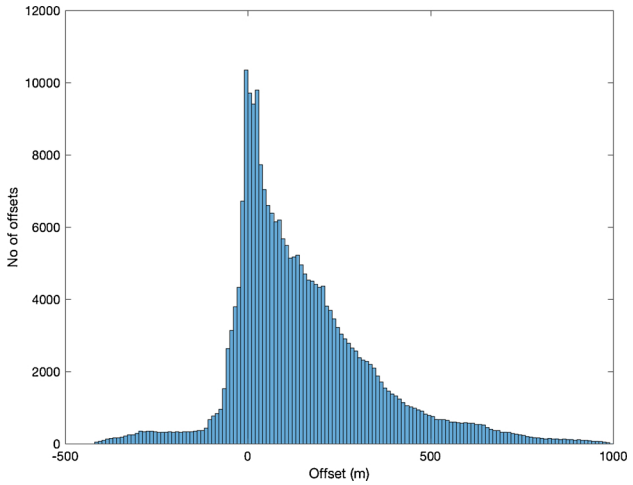

Fig. B2. Crossline offset distribution for the MY101 (1999) survey.

Kirchhoff prestack time-migration using a straight-ray approximation was used to produce the final migrated sections. The resolution of the migration is approximately proportional to the square of the homogeneous Green's function (Thorbecke and Wapenaar, 2007)

$$\Gamma(r,\omega)\tilde{}\frac{sin(kr)}{2\pi r} \tag{B1}$$

Where $k = \omega/c$, ω is the angular frequency, c is the velocity and r is the distance from the image point. For a frequency of 20 Hz, and a velocity of 2000 m/s the area contributing to an image point has a diameter of approximately 100 m.

The effect of cross-line dip and cable feathering on zero-offset traveltime

In the following we consider only the MY101 (1999) survey, since the errors for the D13 (2011) survey are in general less than the 1999 survey.

For our analysis the most critical errors due to inaccurate source and receiver positions are the travel time errors. The travel time τ for a dipping reflector is given by

$$\tau = \sqrt{\tau_0^2 + \frac{h^2}{V_{nmo}^2}}. \tag{B2}$$

where τ_0 is the zero-offset travel time, h is the offset and V_{nmo} is the dip-dependent apparent stacking velocity (Levin, 1971). The zero offset travel time is measured along a ray path normal to the dipping layer and will depend on the midpoint-position. The stacking velocity depends on the dip angle of the reflector and the direction of the survey line. Fig. B8 shows the depth of the seafloor in an area around the survey line. The local dip angles in the in-line and cross-line direction are quite small, less than 10 °, and we can safely ignore the dip dependence and assume that V_{nmo} is the same as the stacking velocity for a plane reflector (Levin, 1971).

An error in the source and receiver position can be described by an error in the offset Δh and an error in the vertical travel time τ_0. The travel time τ depends on the midpoint position only through the zero-offset travel time, hence we can describe the effect of errors in the midpoint position by the equivalent error in the zero-offset travel time.

The error $\Delta\tau$ in the travel time are found by simple sensitivity analysis of Eq. B2 to be

$$\Delta\tau = \frac{\tau_0}{\tau}\Delta\tau_0 + \frac{h}{\tau V_{NMO}^2}\Delta h \tag{B3}$$

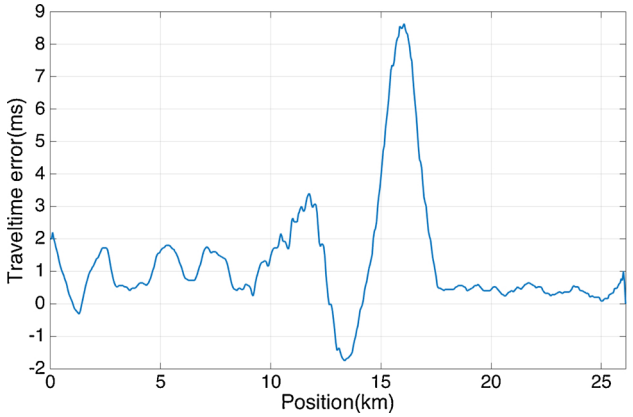

Fig. B3. Travel time error of the sea bottom reflector based on a 3D synthetic dataset. The seismic model used to create the data was built using the bathymetry from the area around the survey line.

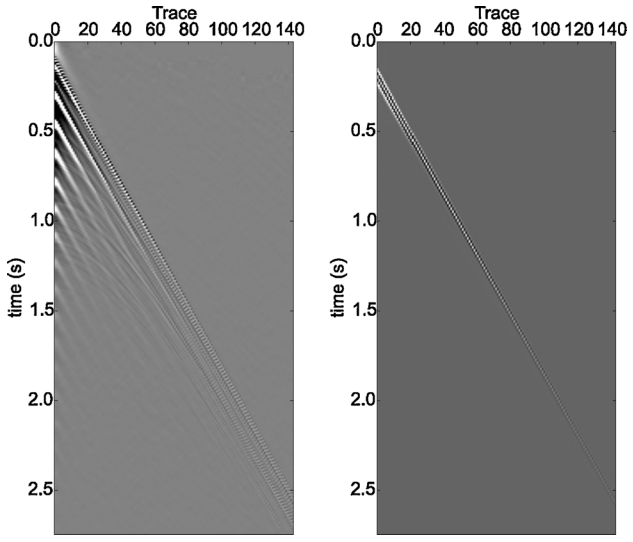

Fig. B4. Input data (left) for estimation of debubble filter. The desired output is shown on the right.

For the processing sequence we are using the zero-offset travel time is controlled by the near offsets. Any errors in the near-offset midpoints will induce errors in the zero-offset travel time due to the varying depth of the dipping reflector. Fig. B9 shows the distribution of midpoint errors in the direction normal to the survey line. In the inline direction the error in the midpoint

position will generally be less than half the receiver distance, which is equal to 12.5 m. The cross-line error is generally less than 100 m, which is within the lateral resolution limit of the prestack time migration.

Figs. B10 and B11 show the distributions of depth differences between the seafloor depth and lines centered on each shot point and extending 100 m in the cross line direction and 25 m meters in the inline direction.

From these figures a reasonable estimate of the depth differences in the inline and cross-line directions are 3 m which combined would give an error of at most 6 m and an error in the zero-offset travel time of

$$\Delta t_0 \leq 2\left(\frac{6}{1500}\right) = 8ms.$$

where we have used a stacking velocity equal to 1500 m/s. This is probably an upper limit, and a more reasonably combined depth difference of 4 m would give a zero-offset travel time error of 5 ms.

Fig. B3 shows the cross-line offset distribution for all offsets. The maximum cross-line offset is about 1000 m, which occurs only for the largest offsets. For a travel time of 3 s, Eq. B3 gives a travel time error of approximately 32 ms at an offset of 3000 m. It is now important to understand that this travel time error does not show up directly in the final migrated sections. This travel time error is manifested as an error in the estimated stacking velocity since Eq. B1 shows that a change in offset is indistinguishable from a change in the stacking velocity and in fact an error in the stacking velocity ΔV_{NMO} gives an error in the travel time as

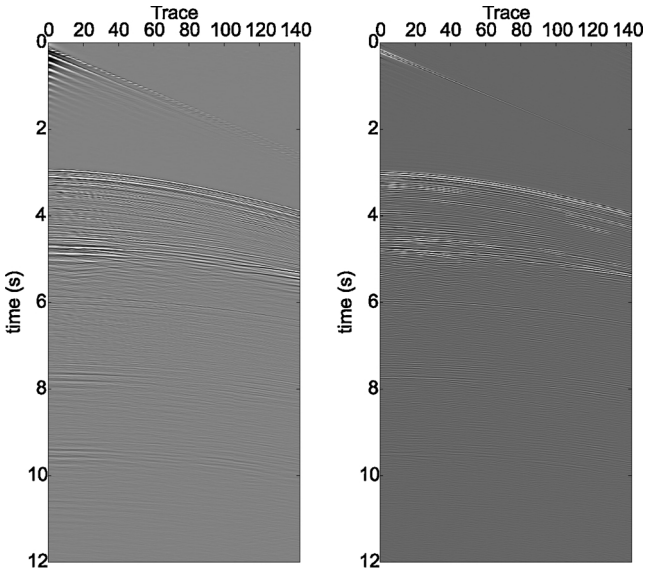

Fig. B5. Input shot (left) and the output after debubble (right).

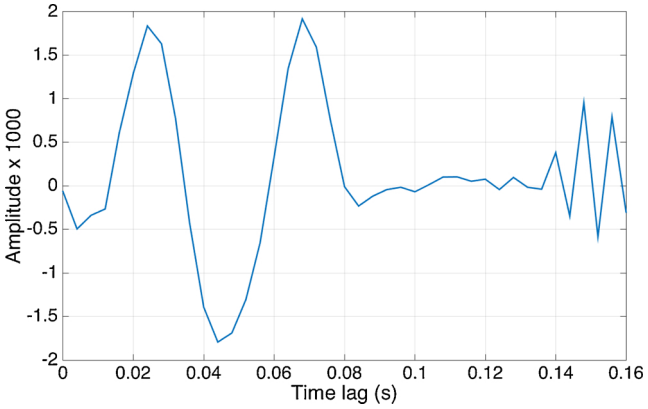

Fig. B6. Global match filter used to match the MY101 (1999) survey to the D13 (2011) survey.

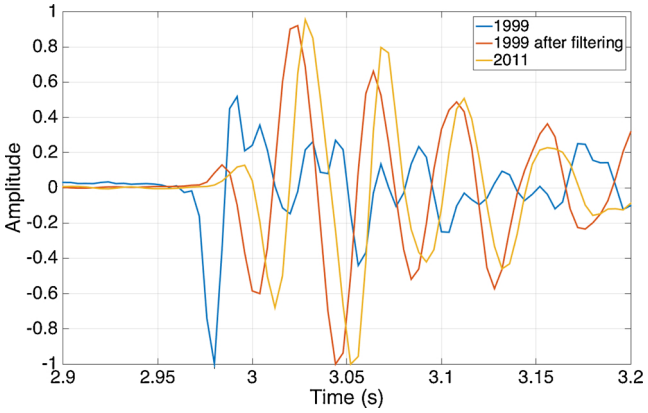

Fig. B7. Comparison of the seabed reflection before and after global matching. The traces have an offset of 150 m and picked from shots at a position of 5 km from the start of the survey.

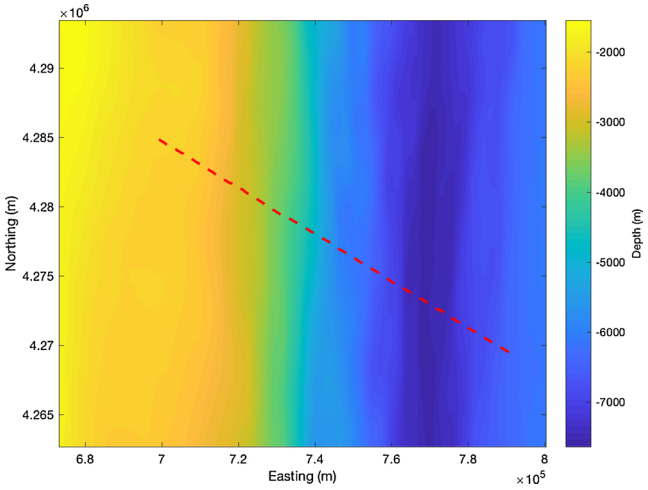

Fig. B8. Bathymetry of the area surrounding the 1997 line. The red dashed line indicates the survey line. (For interpretation of the references to colour in this figure legend, the reader is referred to the web version of this article).

$$\Delta\tau = -\frac{1}{\tau}\frac{h^2}{V_{NMO}^3}\Delta V_{NMO} \tag{B4}$$

Using Eq. (B4) an error in the travel time of 32 ms corresponds to an error of approximately 40 m/s in the stacking velocity. In the final seismic image this will appear as a slight error in the amplitude, the image being slightly defocused. The vertical travel time measured from the seismic section will only be affected by the depth differences due to the error in the near offset midpoints.

We can conclude that the errors in the source and receiver positions will at most imply an error in the zero-offset two-way travel time measured on the seismic section of 8 ms, but more likely is an error of 5 ms. These estimates are in accordance with the results shown in Fig. B3.

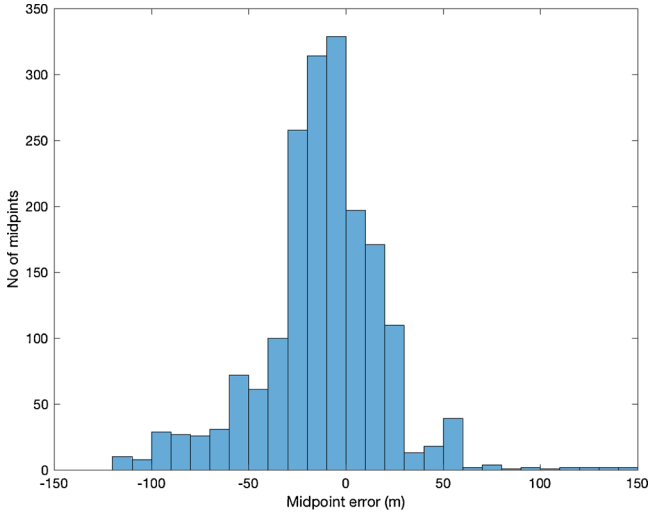

Fig. B9. Near offset midpoint position error in the cross-line direction.

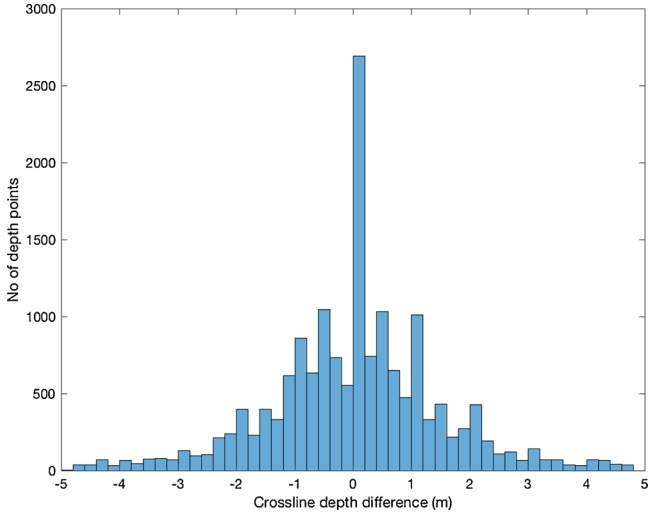

Fig. B10. Seafloor depth differences calculated along lines extending 100 m on each side of survey shot points in the North-South direction. The depth difference is relative to the depth of the seafloor at the survey shot points.

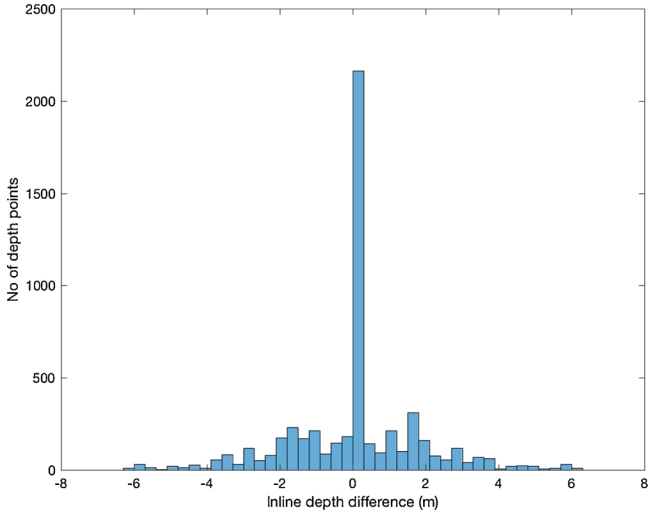

Fig. B11. Seafloor depth differences calculated along lines extending 25 m on each side of survey shot points in the East-West direction. The depth difference is relative to the depth of the seafloor at the survey shot points.

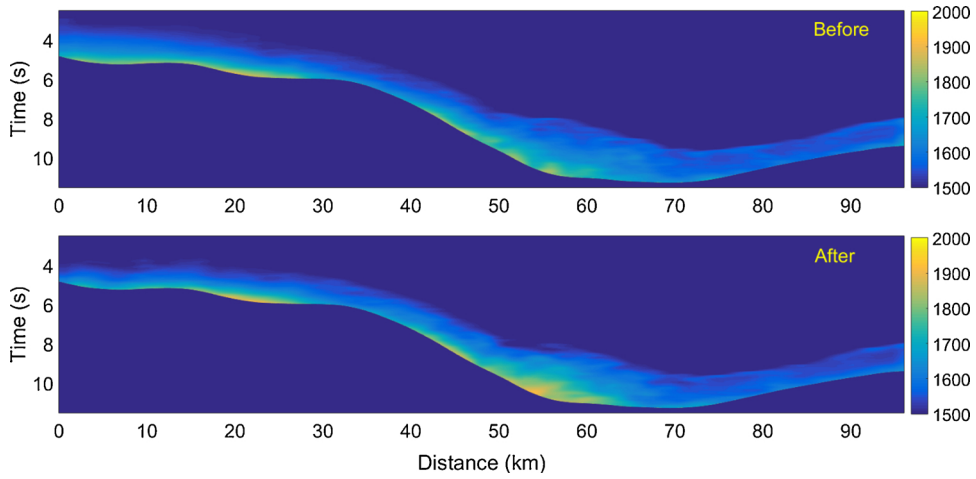

Fig. C1. Stacking velocities before (top) and after (bottom) the earthquake. Notice that the velocities for the sub-sediment rocks have been set to 1500 m/s.

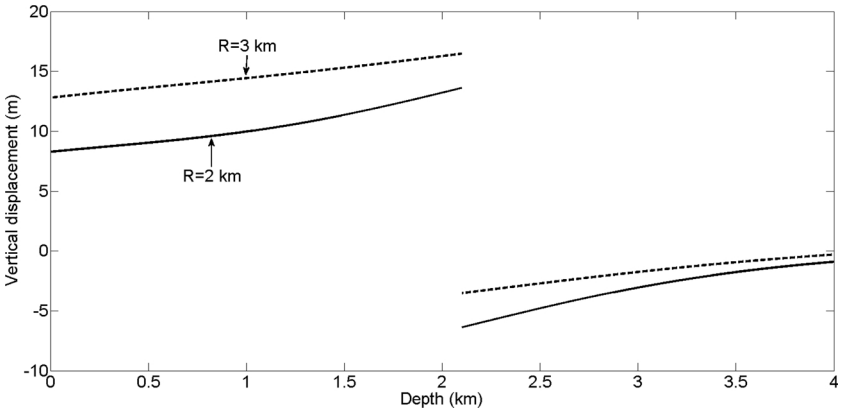

Fig. D1. Modeled vertical displacement versus depth (measured from seabed) using Geertsmaa's equation for a cylinder radius of 2 and 3 km radius, respectively. Here we assume that the sediment package is 2.1 km thick and we observe that a seabed subsidence of 8.2 m corresponds to approximately 13.8 m subsidence at the sediment-basement interface (2.1 km), corresponding to an overburden stretch of 5.6 m. For a 3 km radius, the corresponding stretch is less, 3.8 m. In the modeling we have used $H_0 = 10$ m and a Poisson ratio of 0.25.

Appendix C. Seismic velocity field within sediments

The stacking velocities were estimated using an automatic method suggested by Fomel (2009). Fig. C1 shows the estimated P-wave velocities before and after the earthquake for the upper sediment layers only. The auto-picked velocities were deemed reliable above the basement reflection only. Beneath the basement reflection, the auto picked velocities were deemed as highly uncertain. This is due to the low signal to noise ratios and to the poorly resolved semblance panels for these areas. A manual picking effort has also been carried out for picking the stacking velocities beneath the basement, however for the offset ranges considered in this data the velocities are poorly resolved. Hence, we have chosen to mute the velocities beneath the basement in Fig. C1. The muted velocities have no influence on the results of this work, as only the upper sediment reflections were used in the analysis. It is interesting to observe the increase of high velocities (yellow color) between 50 and 65 km, close to the trench axis. One potential interpretation is that the sediments in this region have been compressed due to an upward force acting towards East and the trench axis.

Appendix D. Geomechanical modeling

Geertsmaa (1973) derived a simple model for geomechanics, the nucleus of strain model. Fjær et al. (2008), gives a simplified approximation of the vertical displacement (u_z) along the center line above a compacting reservoir:

$$u_z = -H_0\left[3 - 4\nu + \frac{d-z}{|d-z|} - \frac{d-z}{\sqrt{r^2+(d-z)^2}} - \frac{(d+z)(3-4\nu)}{\sqrt{r^2+(d+z)^2}} + \frac{2r^2 z}{(r^2+(d+z)^2)^{\frac{3}{2}}}\right], \tag{D1}$$

where ν is the Poisson ratio for the elastic rock, d is the depth of the compacting reservoir, z is the distance from the surface and r is the radius of the reservoir. H_0 is dependent on several rock physics parameters, among them the pore pressure change causing the compaction. However, for our purpose the details of this constant is not crucial, and we will treat this H_0 as an empirical fitting factor in our simple simulations. One example of such a modelling is shown in Fig. D1, assuming reservoir radii of 2 and 3 km, respectively. From such modeling we can estimate the stretch within the sedimentary unit. For a 2 km radius we observe that the overburden stretch is approximately 5–6 m, and that it is reduced to 3–4 m for a radius of 3 km. This modeling is very similar to observations from the Ekofisk reservoir in the North Sea, where the seabed subsidence is up to 9 m caused by the compaction of the chalk reservoir at 3 km depth. Once the stretch is known, we can estimate dz/z and hence we can estimate the R-factor from Eq. 3, since the relative timeshift within the sedimentary layer is known from the time-lapse seismic data. We found an "average" R-factor of approximately 7 that is assumed constant for the first 20 km along the 2D seismic profile. This number is of course very uncertain, since we do not know the radius of the rock units that we assume has been subsiding at the sediment-basement interface. However, this number is in agreement with Hatchell and Bourne (2005) where an overburden R-value of 5 was used.

References

Amundsen, L., Landrø, M., 2010. Marine seismic sources, part 1: air-guns for non experts. GeoExpro 7 (2), 32–35.

Arts, R., Chadwick, A., Eiken, O., Thibeau, S., Nooner, S., 2008. Ten years' experience of monitoring CO_2 injection in the Utsira sand at Sleipner, offshore Norway. First Break. 26, 65–72.

Barkved, O.I., Kristiansen, T., 2005. Seismic time-lapse effects and stress changes: examples from a compacting reservoir. Lead. Edge 24, 1244–1248.

Bergman, P., Yang, C., Lüth, S., Juhlin, C., Cosma, C., 2011. Time-lapse processing of 2D seismic profiles with testing of static correction mehtods at the CO_2 injection site Ketzin (Germany). J. Appl. Geophys. 75, 124–139.

Chen, C.-T., Millero, F.J., 1977. Speed of sound in seawater at high pressures. J. Acoust. Sos. Am. 62, 1129–1135.

Chester, F.M., Rowe, C., Ujiie, K., Kirkpatrick, J., Regalla, C., Remitti, F., Moore, J.C., Toy, V., Wolfson-Schwehr, M., Bose, S., Kameda, J., Mori, J.J., Brodsky, E.E., Eguchi, N., Toczko, S., Expedition 343, 343T Scientists, 2013. Structure and composition of the plate-boundary slip zone for the 2011 Tohoku-Oki earthquake. Science 342 (6163), 1208–1211.

Chu, R., Wei, S., Helmberger, D.V., Zhan, Z., Zhu, L., Kanamori, H., 2011. Initiation of the great M_W 9.0 Tohoku-Oki earthquake. Earth Planet. Sci. Lett. 308, 277–283.

Eiken, O., Tøndel, R., 2005. Sensitivity of time-lapse seismic data to pore pressure changes: Is quantification possible? Lead. Edge 24, 1250–1254.

Fjær, E., Holt, R.M., Horsrud, P., Raaen, A.M., Risnes, R., 2008. Petroleum Related Rock Mechanics, Developments in Petroleum Science 53, 2nd edition. Elsevier 978-0-444-50260-5.

Fofonoff, N.P., Millard Jr., R.C., 1983. Algorithms for computation of fundamental properties of seawater. UNESCO Technical Papers in Marine Science. 44.

Fomel, S., 2009. Velocity analysis using *AB* semblance. Geophys. Prospect. 57, 311–321. https://doi.org/10.1111/j.1365-2478.2008.00741.x.

Fujii, Y., Satake, K., Sakai, S.I., Shinohara, M., Kanazawa, T., 2011. Tsunami source of the 2011 off the Pacific coast of Tohoku Earthquake. Earth Planets Space 63 (7), 815.

Fujiwara, T., Kodaira, S., No, T., Kaiho, Y., Takahashi, N., Kaneda, Y., 2011. The 2011 Tohoku-Oki earthquake: displacement reaching the trench axis. Science 334 (6060) 1240-1240.

Geertsma, J., 1973. A basic theory of subsidence due to reservoir compaction: the heterogeneous case. Verhandelingen Kon. Ned. Geol. Mijnbouwk. Gen 28, 43–62.

Guilbot, J., Smith, B., 2002. 4-D constrained depth conversion for reservoir compaction estimation: application to Ekofisk Field. Lead. Edge 21, 302–308.

Hatchell, P., Bourne, S., 2005. Rocks under strain: strain-induced time-lapse time shifts are observed for depleting reservoirs. Lead. Edge 24, 1222–1225.

Hatchell, P.J., Kawar, R.S., Savitski, A.A., 2005. Integrating 4D seismic, geomechanics and reservoir simulation in the Valhall oil field. 67th Conference and Exhibition, EAGE, Extended Abstracts, C012.

Ide, S., Baltay, A., Beroza, G.C., 2011. Shallow dynamic overshoot and energetic deep rupture in the 2011 Mw 9.0 Tohoku-Oki earthquake. Science 332 (6036), 1426–1429.

Iinuma, T., 2018. Monitoring of the spati-temporal change in the interpolate coupling at northeastern Japan subduction zone based on the spatial gradients of surface velocity field. Geophys. J. Int. 213, 30–47.

IPCC, 2005. In: Metz, B., Davidson, O., de Coninck, H., Loos, M., Meyer, L. (Eds.), Special Report on Carbon Dioxide Capture and Storage. Cambridge University Press ISBN:13 978-0-521-86643-9.

Ito, Y., Tsuji, T., Osada, Y., Kido, M., Inazu, D., Hayashi, Y., Tsushima, H., Hino, R., Fujimoto, H., 2011. Frontal wedge deformation near the source region of the 2011 Tohoku-Oki earthquake. Geophys. Res. Lett. 38https://doi.org/10.1029/2011GL048355. L00G05.

Jiang, J., Simons, M., 2016. Probabilistic imaging of tsunamigenic seafloor deformation during the 2011 Tohoku-oki earthquake. J. Geophys. Res. Solid Earth 121, 9050–9076. https://doi.org/10.1002/2016JB013760.

Jolivet, L., Tamaki, K., 1992. Neogene kinematics in the Japan region and volcanic activity of the northeast Japan arc. Proc. Ocean Drill. Prog. Sci. Results 127/128 (Part 2), 1311–1331.

Juanes, R., Hager, B.H., Herzog, H.J., 2012. No geologic evidence that seismicity causes fault leakage that would render large-scale carbon capture and storage unsuccessful. PNAS 109, E3623.

Kido, M., Osada, Y., Fujimoto, H., Hino, R., Ito, Y., 2011. Trench-normal variation in observed seafloor displacements associated with the 2011 Tohoku-Oki earthquake. Geophys. Res. Lett. 38 (24).

Kodaira, S., No, T., Nakamura, Y., Fujiwara, T., Kaiho, Y., Miura, S., Takahashi, N., Kaneda, Y., Taira, A., 2012. Nat. Geosci. Lett. https://doi.org/10.1038/NGEO1547.

Kodaira, S., Nakamura, Y., Yamamoto, Y., Obana, K., Fujie, G., No, T., Kaiho, Y., Sato, T., Miura, S., 2017. Depth-varying structural characters in the rupture zone of the 2011 Tohoku-oki earthquake. Geosphere. https://doi.org/10.1130/GES01489.1.

Landrø, M., 1999. Repeatability issues of 3D VSP data. Geophysics 64, 1673–1679.

Landrø, M., 2001. Discrimination between pressure and fluid saturation changes from time lapse seismic data. Geophysics 66, 836–844.

Landrø, M., 2011. Seismic monitoring of an old underground blowout – 20 years later. First Break. 29, 39–48.

Landrø, M., 2015. In: Bjørlykke, K. (Ed.), Petroleum Geoscience, 2nd edition. Springer, pp. 489–514. https://doi.org/10.1007/978-3-642-34132-8. Chapter 19.

Landrø, M., Stammeijer, J., 2004. Quantitative estimation of compaction and velocity changes using 4D impedance and traveltime changes. Geophysics 69, 949–957.

Landrø, M., Solheim, O.A., Hilde, E., Ekren, B.O., Strønen, L.K., 1999. The gullfaks 4D study. Pet. Geosci. 5, 213–226.

Landrø, M., Zumberge, M., 2017. Estimating saturation and density changes caused by CO_2 injection at Sleipner – using time-lapse seismic amplitude-variation-with-offset and time-lapse gravity. Interpretation 5, T243–T257.

Lay, T., Ammon, C.J., Kanamori, H., Xue, L., Kim, M.J., 2011. Possible large near-trench slip during the 2011 Mw 9.0 off the Pacific coast of Tohoku Earthquake. Earth Planets Space 63 (7), 687–692.

Lee, W.H.K., Cox, C.S., 1966. Time variation of ocean temperatures and its relation to internal waves and oceanic heat flow measurements. J. Geophys. Res. 71, 2101–2111.

Levin, F.K., 1971. Apparent velocity from dipping interface reflections. Geophysics 36, 510–516.

Mackenzie, K.V., 1981. Nine-term equation for sound speed in the oceans. J. Acoust. Soc. Am. 70, 807–812.

Nedimovic, M.R., West, G.F., 2003. Crooked-line 2D seismic reflection imaging in crystalline terrains: part 1, data processing. Geophysics 68, 274–285.

Osdal, B., Landrø, M., 2011. Estimation of changes in water column velocities and thicknesses from time lapse seismic data. Geophys. Prospect. 59, 295–309.

Røste, T., Stovas, A., Landrø, M., 2005. Estimation of layer thickness and velocity changes using 4D prestack seismic data. 67th Conference and Exhibition, EAGE, Extended Abstracts, C010.

Røste, T., Landrø, M., Hatchell, P., 2007. Monitoring overburden layer changes and fault movements from time-lapse seismic data on the Valhall Field. Geophys. J. Int. 170, 1100–1118.

Røste, T., Dybvik, O.P., Søreide, O.K., 2015. Overburden 4D time shifts induced by reservoir compaction at Snorre field. Lead. Edge 34, 1366–1374. https://doi.org/10.1190/tle34111366.1.

Satake, K., Fujii, Y., Harada, T., Namegaya, Y., 2013. Time and space distribution of coseismic slip of the 2011 Tohoku earthquake as inferred from tsunami waveform data. Bull. Seismol. Soc. Am. 103 (2B), 1473–1492.

Sato, M., Ishikawa, T., Ujihara, N., Yoshida, S., Fujita, M., Mochizuki, M., Asada, A., 2011. Displacement above the hypocenter of the 2011 Tohoku-Oki earthquake. Science 332, 1395.

Shepard, D., 1968. A two-dimensional interpolation function for irregularly-spaced data. Proceedings of the 1968 ACM National Conference. pp. 517–524.

Tamaki, K., Pisciotto, K., Allan, J., 1990. Proc. Ocean Drill. Program Initial Rep. 127, 4.

Tanaka, Y., Sawada, Y., Tanase, D., Tanaka, J., Shiomi, S., Kasukawa, T., 2017. Tomakomai CCS demonstration project of Japan, CO_2 injection in process. Energy Procedia 114, 5836–5846.

Thorbecke, J., Wapenaar, K., 2007. On the relation between seismic interferometry and the migration resolution function. Geophysics 72, T61–T66.

Tsuji, T., Matsuoka, T., Kadir, W.G.A., Hato, M., Takahashi, T., Sule, M.R., Kitamura, K., Yamada, Y., Onishi, K., Widarto, D.S., Sebayang, R.I., Prasetyo, A., Priyono, A., Ariadji, T., Sapiie, B., Widianto, E., Asikin, A.R., Gundih CCS project team, 2014. Reservoir characterization for site selection in the Gundih CCS project, Indonesia. Energy Procedia 63, 6335–6343.

Tsuru, T., Park, J.-O., Miura, S., Kodaira, S., Kido, Y., Hayashi, T., 2002. Along-arc structural variation of the plate boundary at the Japan Trench margin: implication of interpolate coupling. J. Geophys. Res. 107, 2357.

Verdon, J.P., 2014. Significance for secure CO_2 storage of earthquakes induced by fluid injection. Environ. Res. Lett. 9, 064022 (10 pp).

von Huene, R., Culotta, R., 1989. Tectonic erosion at the front of the Japan Trench convergent margin. Tectonophysics 160 (1-4), 75–90.

von Huene, R., Lallemand, S., 1990. Tectonic erosion along the Japan and Peru convergent margins. Geol. Soc. Am. Bull. 102 (6), 704–720.

von Huene, R., Klaeschen, D., Cropp, B., Miller, J., 1994. Tectonic structure across the accretionary and erosional parts of the Japan Trench margin. J. Geophys. Res. Solid Earth 99 (B11), 22349–22361.

Weibull, W.W., Arntsen, B., 2013. Automatic velocity analysis with reverse-time migration. Geophysics 78, S179–S192.

Wong, G.S.K., Zhu, S., 1995. Speed of sound in seawater as a function of salinity, temperature and pressure. J. Acoust. Soc. Am. 97, 1732–1736.

Zadeh, M.H., Landrø, M., 2011. Monitoring a shallow subsurface gas flow by time lapse refraction analysis. Geophysics 76, O35–O43.

Zoback, M.D., Gorelick, S.M., 2012. Earthquake triggering and large-scale geologic storage of carbon dioxide. PNAS 109, 10164–10168.